

Article

# Spectra–Structure Correlations in Isotopomers of Ethanol (CX<sub>3</sub>CX<sub>2</sub>OX; X = H, D): Combined Near-Infrared and Anharmonic Computational Study

Krzysztof B. Beć<sup>1,2,\*</sup> , Justyna Grabska<sup>1</sup>, Christian W. Huck<sup>1</sup>  and Mirosław A. Czarnecki<sup>2</sup>

<sup>1</sup> Institute of Analytical Chemistry and Radiochemistry, Leopold-Franzens University, Innrain 80/82, CCB-Center for Chemistry and Biomedicine, 6020 Innsbruck, Austria; Justyna.Grabska@uibk.ac.at (J.G.); Christian.W.Huck@uibk.ac.at (C.W.H.)

<sup>2</sup> Faculty of Chemistry, University of Wrocław, F. Joliot-Curie 14, 50-383 Wrocław, Poland; mirosław.czarnecki@chem.uni.wroc.pl

\* Correspondence: Krzysztof.Bec@uibk.ac.at; Tel.: +43-512-507-5783

Academic Editor: Fabrizio Santoro

Received: 8 May 2019; Accepted: 8 June 2019; Published: 11 June 2019



**Abstract:** The effect of isotopic substitution on near-infrared (NIR) spectra has not been studied in detail. With an exception of few major bands, it is difficult to follow the spectral changes due to complexity of NIR spectra. Recent progress in anharmonic quantum mechanical calculations allows for accurate reconstruction of NIR spectra. Taking this opportunity, we carried out a systematic study of NIR spectra of six isotopomers of ethanol (CX<sub>3</sub>CX<sub>2</sub>OX; X = H, D). Besides, we calculated the theoretical spectra of two other isotopomers (CH<sub>3</sub>CD<sub>2</sub>OD and CD<sub>3</sub>CH<sub>2</sub>OD) for which the experimental spectra are not available. The anharmonic calculations were based on generalized vibrational second-order perturbation theory (GVPT2) at DFT and MP2 levels with several basis sets. We compared the accuracy and efficiency of various computational methods. It appears that the best results were obtained with B2PLYP-GD3BJ/def2-TZVP//CPCM approach. Our simulations included the first and second overtones, as well as binary and ternary combinations bands. This way, we reliably reproduced even minor bands in the spectra of diluted samples (0.1 M in CCl<sub>4</sub>). On this basis, the effect of isotopic substitution on NIR spectra of ethanol was accurately reproduced and comprehensively explained.

**Keywords:** near-infrared spectroscopy; ethanol; anharmonic quantum mechanical calculations; isotopic substitution; overtones; combinations bands

## 1. Introduction

Near-infrared (NIR) spectra are appreciably more complex and difficult for interpretation than IR or Raman spectra [1–6]. This results from a large number of strongly overlapping overtones and combination bands, numerous resonances between different modes and anharmonicity of vibrations [1–6]. Interpretation of vibrational bands has been aided by studies of a series of similar compounds (including isotopomers), or by reconstruction of the spectra by using quantum mechanical calculations [5]. The former way may provide highly speculative assignments, while the latter method has limitations that prevent their common use in NIR spectroscopy. From the point of view of applied spectroscopy, there exists an essential difference in the applicability of quantum mechanical calculation of mid-infrared (MIR) [7–9] and NIR spectra. A simplistic and computationally inexpensive harmonic approximation fails to predict the overtones and combination modes [10]. Because of a considerable computational cost of anharmonic calculations, simulations of NIR spectra are rare. Nevertheless, in the literature one can find examples of application of different approaches used for calculation of overtones

and combination bands, including variational approaches, which are expensive but useful in selected cases [11,12]. However, the studies using a vibrational self-consistent field (VSCF) approach [13,14] and its refined variants—e.g., PT2-VSCF—are more common [15–17]. Recently, a number of theoretical reconstructions of NIR spectra by means of efficient vibrational second-order perturbation (VPT2) method have been reported [18]; e.g., carboxylic acids [19], fatty acids [20–22], aminoacids [23], nucleobases [24], nitriles [25], azines [26], phenols [27,28], and alcohols [29,30]. Considerable efforts have been undertaken in order to develop anharmonic approaches applicable to even larger molecular systems [31–34]. On the other hand, meticulous probing of vibrational potential capable of yielding nearly-exact results is also available [35–38]. Recent advances in this field include the development of multi-dimensional approaches that provide complete information on mode couplings in linear triatomic molecules [39].

The isotopic effect appears to be helpful for the analysis of NIR spectra [10]. By shifting a part of overlapped contributions, one can reduce their complexity and reveal individual bands. Time-resolved NIR spectroscopy of deuterated alcohols has also been successfully used for elucidating the diffusion coefficients [40]. In our previous work, the effect of isotopic substitution on NIR spectra of methanol has been accurately reproduced by anharmonic calculations [41]. In particular, we were able to predict the vibrational contributions from non-uniformly substituted  $CX_3OX$  ( $X = H, D$ ) species, which are not available from the experiment [41]. Further studies on molecules more complex than methanol are still necessary. A reasonable progress in this field is expected by examination of ethanol and all its isotopomers [42,43]. Ethanol has eight major isotopomers resulting from deuteration ( $CX_3CX_2OX$ ;  $X = H, D$ ), as compared to four in methanol. Moreover, the internal rotation around C-O(H) bond leads to rotational isomerism (*gauche*, *trans*) in molecules of ethanol, which adds additional origin of spectral variability in NIR spectra [42,43].

To enable detailed examination of the impact of various effects on NIR spectra of ethanol isotopomers, at first it is necessary to perform reliable theoretical reproduction of NIR spectra for eight isotopomers of ethanol ( $CX_3CX_2OX$ ;  $X = H, D$ ). We are interested in accurate reproduction of subtle effects observed in NIR spectra. Therefore, a combination of several electronic methods underlying VPT2 vibrational analysis will be useful for establishing the best approach capable of reproducing fine features in NIR spectra. The determination of electronic structure underlying the geometry optimization and harmonic analysis will be based on Møller–Plesset second-order perturbation (MP2) and density functional (DFT) theories. The efficiency and accuracy of reproduction of NIR bands by MP2 and DFT with single-hybrid B3LYP and double-hybrid B2PLYP density functionals will be overviewed. MP2 and DFT calculations included basis sets of increasing quality (6-31G(d,p), SNST, def2-TZVP, and aug-cc-pVTZ). Moreover, the impact of solvent cavity model will be evaluated. The anharmonic vibrational analysis will be carried out by means of generalized VPT2 (GVPT2). In our previous studies on methanol, it has been demonstrated that the relative contributions from the second overtones and ternary combinations are different for various isotopomers [41]. This work will provide detailed information on contributions from different vibrational modes and the trends observed with increasing of the alkyl chain length in going from methanol to ethanol. In addition, we will elucidate the accuracy of prediction of the three quanta transitions in NIR spectra.

## 2. Results and Discussion

### 2.1. Accuracy of Reproduction of NIR Spectra by Selected Approaches

Anharmonic calculations are significantly more challenging compared to harmonic approximation [1–4]. This holds even for efficient anharmonic approaches based on VPT2 method. At the same time, the higher quanta transitions are more prone to inaccuracies than the fundamental ones [44]. An insufficient accuracy of the ground state geometry and potential energy surface may easily propagate into inaccuracy of prediction in VPT2 calculation step. Thus, the theoretical prediction of NIR

spectra is usually a compromise between the cost and accuracy. Effects like isotopic substitution [41] and conformational isomerism [29,30] may further complicate the vibrational analysis of NIR spectra.

One of the aims of this work was assessment of the efficiency of several combinations of the electronic theory methods and basis sets (Table 1). In addition, we examined the effect of the solvent model on the anharmonic vibrational energies. An efficient single-hybrid B3LYP functional is commonly used tool for spectroscopic studies [10]. Empirical correction for dispersion has been introduced to overcome one of the major weaknesses of DFT method [45]. In some cases, this approach markedly improves the robustness of calculation of primary parameters (i.e., energy). Therefore, recent literature suggests employing empirical correction for dispersion in DFT calculations [46]. Our previous studies have shown that, even for small and isolated molecules, this correction is advantageous in spectra modeling [29]. For molecules in solution an approximation of the solvent cavity often improves the quality of the simulated NIR spectra [28]. However, in the present work this advantage is less important (Table 1). We observed an improvement of RMSE from 45 to 35  $\text{cm}^{-1}$  for  $\text{CH}_3\text{CH}_2\text{OH}$ , and from 27 to 24  $\text{cm}^{-1}$  for  $\text{CH}_3\text{CH}_2\text{OD}$ . However, considering small additional cost of CPCM (ca. 10% of total CPU time in the case of GVPT2//B3LYP-GD3BJ/6-31G(d,p) calculations), it is advisable to include this correction step in the calculations.

Switching from B3LYP to B2PLYP density functional with a small basis set (6-31G(d,p)) leads to an increase in the RMSE value (Table 1). However, B2PLYP method overestimated the band positions in a systematic manner. In contrast, B3LYP approach provides irregular results. Some of the band positions ( $\delta\text{CH}$ ) are blue-shifted, while the others ( $\nu\text{OX}$  and  $\nu\text{CX}$ ; X = H, D) are red-shifted. Thus, more uniform band shift from B2PLYP method (Figures 1 and 2) resulted in better interpretability of NIR spectra as compared with B3LYP results. It has a peculiar effect in NIR spectra of aliphatic alcohols, as it reduces RMSE of NIR band positions, particularly for the  $\nu\text{OX} + \delta\text{CH}$ , and  $\nu\text{CX} + \delta\text{CH}$  combination bands. However, this apparent gain does not improve the true interpretability of the spectra. It is likely that simulated NIR spectra of larger molecules may suffer even more due to binary combinations involving the stretching and deformation of the C-H and O-H vibrations. Similar inconsistency of B3LYP as compared to B2PLYP has been noted before [29,41]. Due to electron correlation being computed effectively at the MP2 level, it is commonly accepted that B2PLYP functional requires larger basis sets. B2PLYP coupled with large def2-TZVP basis set noticeably improves the quality of simulated NIR spectra (Figures 1 and 2). This improvement is particularly evident in the reproduction of minor bands originating from the three quanta transitions (Figures 3 and 4). This effect is nicely illustrated by reduction of RMSE from 72–83  $\text{cm}^{-1}$  for B2PLYP/6-31G(d,p) to 18–19  $\text{cm}^{-1}$  for B2PLYP/def2-TZVP. SNST basis set, less complex than def2-TZVP but still of triple- $\zeta$  quality, leads to worse results. An exception was observed for the prominent doublet from the  $\nu\text{CH}$  combination bands (at ca. 4400  $\text{cm}^{-1}$ ), where B2PLYP/SNST calculations reproduced the peak shapes more resembling the experimental ones. However, the position of this doublet was also overestimated by this method. Hence, B2PLYP/def2-TZVP method appears to be the better tool for reliable reconstruction of NIR spectra. A similar conclusion was obtained for butyl alcohols [30].

In contrast, MP2 method does not appear to be particularly useful for anharmonic calculations of NIR spectra of ethanol isotopomers due to significant redshift of the  $\nu\text{CX}$  frequencies (Figures 1 and 2). It is an interesting observation, as the tendency of MP2 to describe incorrectly repulsive forces is known in the literature [47]. In this work, however, an insufficient basis set (6-31G(d,p)) may strongly deviate the results. Here, MP2 method seems to be more sensitive to the effect of a small basis set than DFT-B2PLYP method. As expected, an application of a larger basis set, e.g., aug-cc-pVTZ, improves the accuracy of calculations. However, these results are not as good as those obtained from B2PLYP/def2-TZVP method. Moreover, this improvement is accompanied by a substantial increase of computing time (by ca. 4 times). Nevertheless, selected spectral ranges ( $\nu\text{OH} + \delta\text{CH} \approx 5050\text{--}4800 \text{ cm}^{-1}$  and  $\nu\text{CH} + \delta\text{CH}$  doublet  $\approx 4400 \text{ cm}^{-1}$ ) were better reproduced by MP2/aug-cc-pVTZ computations. Therefore, MP2 approach may be recommended as a reference method in selected cases. Our results demonstrate that different computational methods achieve different accuracy for particular regions of

NIR spectra, and these regions do not overlap. Thus, comparison of the spectra simulated by different methods (e.g., resulting from VPT2 calculations at DFT or MP2 levels) appears to be the best way for reliable interpretation of the experimental spectra.

Particular attention should be paid to  $2\nu\text{OH}/\text{OD}$  band, which is the most characteristic peak for alcohols and the other important compounds like, e.g., phenols [27], terpenes [28], and polyphenols [48]. This peak is very sensitive to the chemical environment and inter- and intra-molecular interactions, and is frequently used for studies of the structure and physicochemical properties [49–53]. Hence, its proper theoretical reproduction is of essential importance. As shown in Figures 1–4, and Figures S1–S6 in SM, most of the methods did not reproduce correctly the shape of this band. The experimental band from  $2\nu\text{OH}/\text{OD}$  vibration reveals a slight asymmetry. This asymmetry is a result of convolution of two components due to *trans* and *gauche* conformers. The lower-frequency *gauche* component has also the lower intensity. Among isotopomers of ethanol, this feature was reproduced correctly only by B2PLYP/def2-TZVP method. MP2/6-31G(d,p) and MP2/aug-cc-pVTZ methods predicted correct shape of the  $2\nu\text{OH}/\text{OD}$  peak only for  $\text{CH}_3\text{CD}_2\text{OH}$  and  $\text{CD}_3\text{CD}_2\text{OD}$ . As can be seen (Table 1), the peak position was overestimated by all used methods, but B2PLYP calculations give the best agreement.

In comparison with other modes, large amplitude motions (LAMs)—e.g., torsion modes and hindered rotations—are more difficult for accurate description in harmonic approximation and also by anharmonic approaches that probe the potential curve relatively shallow (e.g., VPT2) [54]. We did not find any evidence that these low-frequency modes influence NIR bands directly (i.e., their overtone and combination modes do not appear in NIR region). However, a NIR spectrum provides some insights on LAMs as well. In our case, the shape of the  $2\nu\text{OH}/\text{OD}$  band is an indirect probe of the accuracy of prediction of the low-frequency modes. The shape of this band results from two components due to *gauche* and *trans* rotational conformers. Unreliable theoretical abundances of these forms would result in biased relative intensities of the  $2\nu\text{OH}/\text{OD}$  components (Table S1). Gibbs free energies may be affected by erroneous LAMs, which would propagate into incorrect relative abundances of *gauche* and *trans* conformers. Because it is an isolated band of strong intensity, the simulated  $2\nu\text{OH}/\text{OD}$  may be used to assess the reliability of prediction of LAMs and the related Gibbs free energies. This kind of error would manifest itself as a distorted shape of simulated  $2\nu\text{OH}/\text{OD}$  band. Above effect can be seen for some of the methods used in this study, e.g., for B3LYP (B3LYP-GD3BJ/6-31G(d,p); B3LYP-GD3BJ/6-31G(d,p)//CPCM; B3LYP-GD3BJ/SNST//CPCM;) and B2PLYP coupled with an insufficient basis set (B2PLYP-GD3BJ/6-31G(d,p)//CPCM;). However, the methods which yielded the most accurate spectra in the other regions (B2PLYP/def2-TZVP; MP2/6-31G(d,p); MP2/aug-cc-pVTZ) also reproduced  $2\nu\text{OH}/\text{OD}$  peak accurately (Figures 1 and 2). Therefore, we conclude that the LAMs of ethanol and its derivatives were determined adequately by MP2 method. B2PLYP method also provides correct results, but it is more sensitive to the selection of a basis set. On the other hand, B3LYP tends to falsify the Gibbs free energies corrected by anharmonic ZPE. Further studies are needed to determine, whether this effect occurs because of an unreliable description of LAMs. On the other hand, inaccuracy of the  $2\nu\text{OH}/\text{OD}$  frequencies prediction by VPT2 may also be considered as another contributing factor, as we have evidenced such occurrence in the case of the conformers of cyclohexanol [27]. Note that B3LYP functional coupled with a relatively simple basis set yields reasonable reproduction of NIR spectra and correctly predicts the effects of isotopic substitution at a relatively modest computational expense (Figures 1–4 and Figures S1–S6 in SM). However, a tendency to over- and underestimate the position and intensity of some bands may be unfavorable for the reliable interpretation of theoretical NIR spectra. For exploration of more subtle effects, B2PLYP functional seems to be more suitable. In the present study of isotopic substitution and the other effects (e.g., rotational isomerism) on NIR spectra of ethanol, we used B2PLYP/def2-TZVP method with additions of GD3BJ and CPCM.

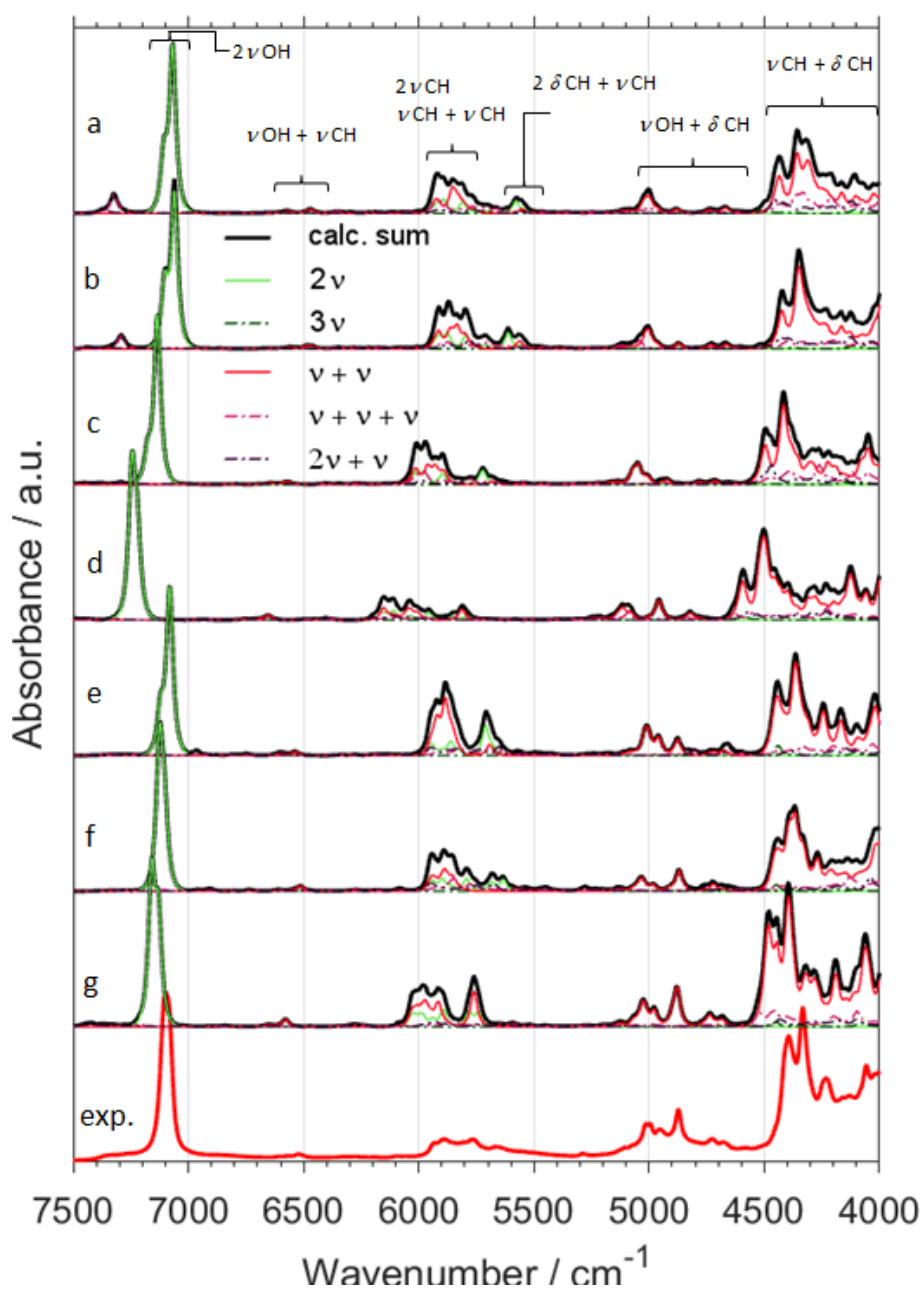


**Figure 1.** NIR spectra of  $\text{CH}_3\text{CH}_2\text{OH}$  calculated with GVPT2 method at different levels of electronic theory; (a) B3LYP-GD3BJ/6-31G(d,p); (b) B3LYP-GD3BJ/6-31G(d,p)//CPCM; (c) B2PLYP-GD3BJ/6-31G(d,p)//CPCM; (d) MP2/6-31G(d,p)//CPCM; (e) B3LYP-GD3BJ/SNST//CPCM; (f) B2PLYP-GD3BJ/def2-TZVP//CPCM; (g) MP2/aug-cc-pVTZ//CPCM; (exp.) Experimental spectrum of  $\text{CH}_3\text{CH}_2\text{OH}$  in  $\text{CCl}_4$  (0.1 M).

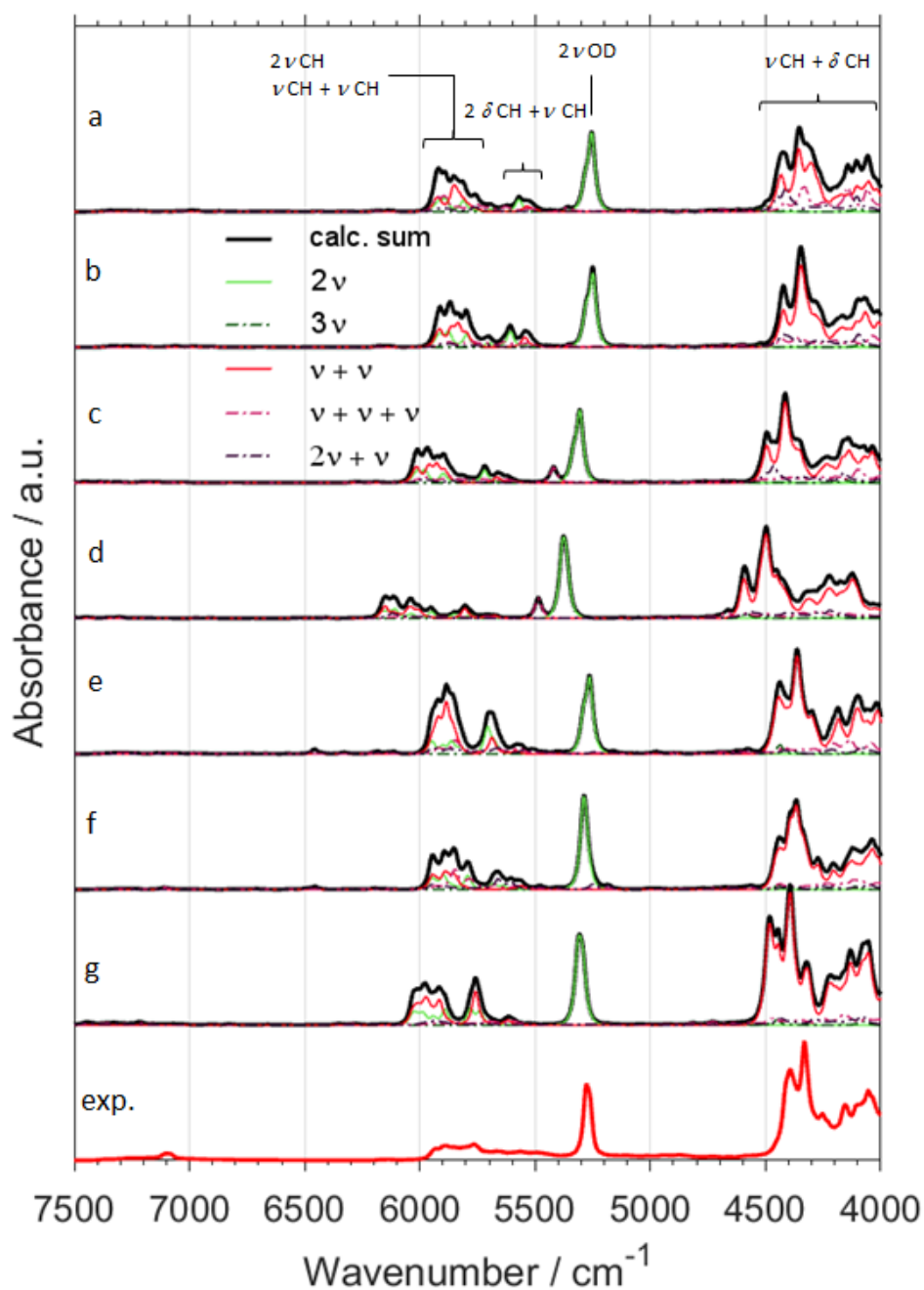


**Figure 2.** NIR spectra of  $\text{CH}_3\text{CH}_2\text{OD}$  calculated with GVPT2 method at different levels of electronic theory; (a) B3LYP-GD3BJ/6-31G(d,p); (b) B3LYP-GD3BJ/6-31G(d,p)//CPCM; (c) B2PLYP-GD3BJ/6-31G(d,p)//CPCM; (d) MP2/6-31G(d,p)//CPCM; (e) B3LYP-GD3BJ/SNST//CPCM; (f) B2PLYP-GD3BJ/def2-TZVP//CPCM; (g) MP2/aug-cc-pVTZ//CPCM; (exp.) Experimental spectrum of  $\text{CH}_3\text{CH}_2\text{OD}$  in  $\text{CCl}_4$  (0.1 M).

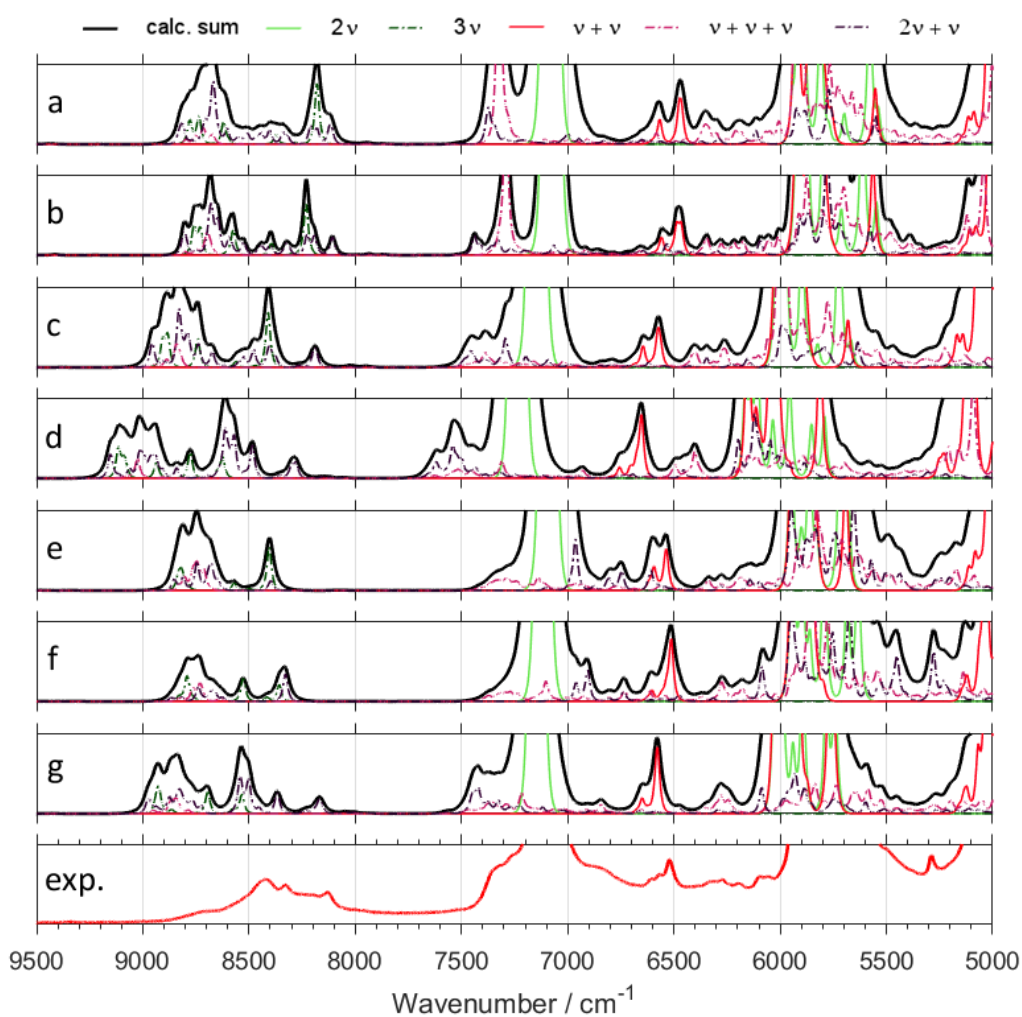


**Figure 3.** Contributions from minor bands in NIR spectra of  $\text{CH}_3\text{CH}_2\text{OH}$  calculated with GVPT2 method at different levels of electronic theory; (a) B3LYP-GD3BJ/6-31G(d,p); (b) B3LYP-GD3BJ/6-31G(d,p)//CPCM; (c) B2PLYP-GD3BJ/6-31G(d,p)//CPCM; (d) MP2/6-31G(d,p)//CPCM; (e) B3LYP-GD3BJ/SNST//CPCM; (f) B2PLYP-GD3BJ/def2-TZVP//CPCM; (g) MP2/aug-cc-pVTZ//CPCM; (exp.) Experimental spectrum of  $\text{CH}_3\text{CH}_2\text{OH}$  in  $\text{CCl}_4$  (0.1 M).

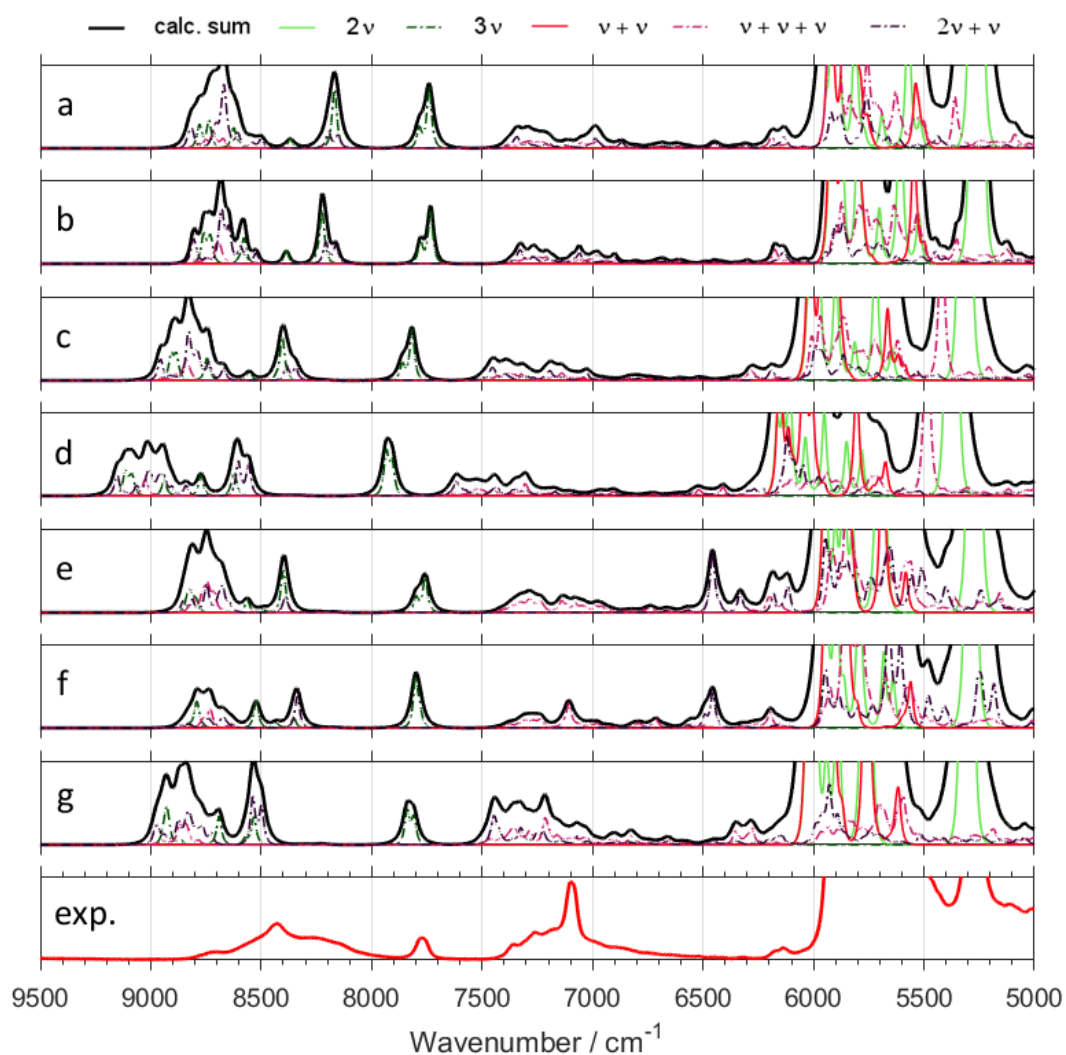


**Figure 4.** Contributions from minor bands in NIR spectra of  $\text{CH}_3\text{CH}_2\text{OD}$  calculated with GVPT2 method at different levels of electronic theory; (a) B3LYP-GD3BJ/6-31G(d,p); (b) B3LYP-GD3BJ/6-31G(d,p)//CPCM; (c) B2PLYP-GD3BJ/6-31G(d,p)//CPCM; (d) MP2/6-31G(d,p)//CPCM; (e) B3LYP-GD3BJ/SNST//CPCM; (f) B2PLYP-GD3BJ/def2-TZVP//CPCM; (g) MP2/aug-cc-pVTZ//CPCM; (exp.) Experimental spectrum of  $\text{CH}_3\text{CH}_2\text{OD}$  in  $\text{CCl}_4$  (0.1 M).

**Table 1.** Positions of selected NIR bands (in  $\text{cm}^{-1}$ ) from GVPT2 anharmonic vibrational analysis in  $\text{CH}_3\text{CH}_2\text{OH}$  and  $\text{CH}_3\text{CH}_2\text{OD}$  at different levels of electronic theory and corresponding RMSE values.

Assignment	Exp.	Calculated													
		MP2/ aVTZ + CPCM	Diff.	B2PLYP- GD3BJ/ def2-TZVP + CPCM	Diff.	B2PLYP- GD3BJ/ SNST + CPCM	Diff.	MP2/ 6-31G(d,p) + CPCM	Diff.	B2PLYP- GD3BJ/ 6-31G(d,p) + CPCM	Diff.	B3LYP- GD3BJ/ 6-31G(d,p) + CPCM	Diff.	B3LYP- GD3BJ/ 6-31G(d,p)	Diff.
$\text{CH}_3\text{CH}_2\text{OH}$															
$2\nu\text{OH}$	7099	7157	58	7125	26	7081	−18	7243	144	7134	35	7061	−38	7096	−3
$\nu_s\text{CH}_2 + \nu\text{OH}$	6520.4	6578	57.6	6513	−7.4	6536	15.6	6654	133.6	6576	55.6	6477	−43.4	6472	−48.4
$2\delta_{as'}\text{CH}_3 + \nu\text{OH}$	5886.1	5980	93.9	5889	2.9	5922	35.9	6111	224.9	5970	83.9	5871	−15.1	5892	5.9
$2\nu_{as}\text{CH}_2$	5765.7	5897	131.3	5790	24.3	5864	98.3	5957	191.3	5898	132.3	5797	31.3	5812	46.3
$2\nu_s\text{CH}_2; 2\nu_s\text{CH}_3 + \delta_s\text{CH}_3$	5665.1	5759	93.9	5681	15.9	5708	42.9	5812	146.9	5722	56.9	5611	−54.1	5768	102.9
$[\delta_{wagg}\text{CH}_2, \delta_s\text{CH}_3] + \nu\text{OH}$	5013.8	5026	12.2	5029	15.2	5012	−1.8	5114	100.2	5049	35.2	5040	26.2	5019	5.2
$[\delta_{twist}\text{CH}_2, \delta_{ip}\text{COH}, \delta_{wagg}\text{CH}_2] + \nu\text{OH}$	4954.2	4978	23.8	4979	24.8	4959	4.8	5003	48.8	5009	54.8	5008	53.8	5003	48.8
$\delta_{ip}\text{COH} + \nu\text{OH}$	4873	4881	8	4868	−5	4877	4	4958	85	4926	53	4874	1	4883	10
$\delta_s\text{CH}_3 + \nu_{as'}\text{CH}_3$	4394.8	4448	53.2	4366	−28.8	4443	48.2	4592	197.2	4473	78.2	4424	29.2	4436	41.2
$[\delta_{oop}\text{COH}, \tau\text{CC}] + \nu\text{OH}$	4333.5	4395	61.5	4331	−2.5	4364	30.5	4502	168.5	4416	82.5	4353	19.5	4357	23.5
		<b>RMSE</b>	70.0	<b>RMSE</b>	18.1	<b>RMSE</b>	40.8	<b>RMSE</b>	153.1	<b>RMSE</b>	72.2	<b>RMSE</b>	35.0	<b>RMSE</b>	44.6
$\text{CH}_3\text{CH}_2\text{OD}$															
$2\nu_{as}\text{CH}_3$	5885.2	5978	92.8	5895	9.8	5921	35.8	6114	228.8	5967	81.8	5871	−14.2	5894	8.8
$2\nu_{as}\text{CH}_2$	5765.6	5917	151.4	5788	22.4	5862	96.4	6007	241.4	5896	130.4	5799	33.4	5815	49.4
$2\nu\text{OD}$	5277.1	5312	34.9	5289	11.9	5265	−12.1	5378	100.9	5306	28.9	5250	−27.1	5255	−22.1
$\delta_{sciss}\text{CH}_2 + \nu_{as}\text{CH}_2$	4393.7	4445	51.3	4397	3.3	4439	45.3	4592	198.3	4493	99.3	4422	28.3	4424	30.3
$[\delta_s\text{CH}_3, \delta_{wagg}\text{CH}_2] + \nu_{as}\text{CH}_3$	4331.8	4392	60.2	4364	32.2	4364	32.2	4500	168.2	4415	83.2	4349	17.2	4355	23.2
$[\delta_{rock}\text{CH}_2, \delta_{rock}\text{CH}_3] + \nu_s\text{CH}_2$	4054.1	4057	2.9	4037	−17.1	4020	−34.1	4122	67.9	4036	−18.1	4068	13.9	4058	3.9
		<b>RMSE</b>	80.6	<b>RMSE</b>	18.6	<b>RMSE</b>	50.0	<b>RMSE</b>	179.4	<b>RMSE</b>	83.3	<b>RMSE</b>	23.6	<b>RMSE</b>	27.3

## 2.2. Origins of NIR Bands of $CX_3CX_2OX$ ( $X = H, D$ )

The simulations of NIR spectra of ethanol isotopomers in  $CCl_4$  solutions by GVPT2 anharmonic method at B2PLYP-GD3BJ/def2-TZVP//CPCM level accurately reproduced most of the experimental bands (Figures 5 and 6). On this basis, we performed detailed and reliable band assignments (Tables 2–9). The consistency of these assignments was positively verified by comparison with the experimental spectra of six isotopomers. High accuracy of simulations allows to analyze the theoretical spectra of  $CH_3CD_2OD$  and  $CD_3CH_2OD$  (Figure 6C,D and Tables 8 and 9) which are not available commercially. All assignments were supported by an analysis of the potential energy distributions (PEDs; Tables S2–S9).

NIR spectra of ethanol isotopomers mainly consist of the combinations of stretching and bending OX and CX ( $X = H, D$ ) modes (Figures 1–6 and Tables 2–9). The region below  $5500\text{ cm}^{-1}$  for  $CH_3CH_2OH$  is almost entirely contributed by the combination bands, while absorption from the overtones dominates above  $5500\text{ cm}^{-1}$ . NIR spectrum of ethanol may be roughly divided into four regions, but only two of them contain meaningful contributions from overtones. These regions are contributed mainly by vibrations from: (1)  $2\nu OX$ ; (2)  $2\nu CX$  and  $\nu CX + \nu CX$ ; (3)  $\nu OX + \delta CX$ ; (4)  $\nu CX + \delta CX$ ; ( $X = H, D$ ). The other combination bands like  $\nu OX + \nu CX$ , and  $2\delta CX + \nu CX$  have low intensity. Isotopic substitution introduces significant band shift, strongly affecting the appearance of NIR spectra (Figures 5 and 6 and Figures S1–S6). It should be noted, that the region of  $5700\text{--}5400\text{ cm}^{-1}$  for ethanols containing  $CH_3$  and  $CH_2$  groups is strongly affected by the anharmonic effects. This effect is well seen for  $CH_3CH_2OH$  (Figure 1) and  $CH_3CH_2OD$  (Figure 2). The most meaningful contributions in this region originate from  $\nu CH + \nu CH$  ( $\nu_{as}CH_2 + \nu_sCH_2$ ),  $2\delta CH + \nu CH$ , and  $2\nu_{as}CH_2$  vibrations as well.

One can notice the overestimated intensities of the  $2\nu CH$  and  $\nu CH + \nu CH$  bands appearing in the  $6000\text{--}5500\text{ cm}^{-1}$  region (Figures 5 and 6 and Figures S1–S6). The magnitude of this effect varies between the different methods; however, it is present in all cases. A similar overestimation we have observed for butyl alcohols [30]. At present, we are unable to explain the reasons for these overestimations. Unexpectedly, B2PLYP functional (regardless of basis set; 6-31G(d,p), SNST, and def2-TZVP yielded similar results) significantly overestimates the frequencies of  $2\delta CH + \delta CH$  transitions, shifting them to the  $5500\text{ cm}^{-1}$  region. In contrast, the most of other transitions in NIR region is accurately reproduced by this approach. In the case of the  $2\delta CH + \delta CH$  modes, large positive anharmonic constants appeared in GVPT2 vibrational analysis. Consequently, positions of the corresponding bands were predicted far from a simple combination of the harmonic frequencies. This shift has not been observed for the remaining approaches. Presently, the reason of this behavior is not clear. Because of very low intensity of  $2\delta CH + \delta CH$  bands, these erroneous predictions do not provide meaningful contributions to NIR spectra. However, this occurrence demonstrates the need for using more than one method during examination of the fine spectral effects.

The deuteration of the OH group leads to a noticeable shift of the  $\nu OD + \delta CH$  band. In contrast, the other bands do not shift meaningfully, as can be easily seen from comparison of  $CH_3CH_2OH$  and  $CH_3CH_2OD$  spectra (Figure 5A,B). In particular, the absorption from the  $\nu CH + \delta CH$  in the  $4600\text{--}4000\text{ cm}^{-1}$  region remains unaffected. This region can be used to monitor the isotopic substitutions of the  $CH_3$  and  $CH_2$  groups, as it leads to highly specific spectral changes. Obviously, simultaneous deuteration of both groups implies more significant changes. However, the most interesting effects result from the selective substitution of one of these groups. The presence of the  $CH_3$  group gives rise to a prominent doublet near  $4395$  and  $4330\text{ cm}^{-1}$ . This doublet has a complex structure resulting from overlapping of the contributions from the  $CH_2$  (Figure S7 in Supplementary Material), leading to a broadening of the high-frequency wing of the doublet. As expected, this contribution is not present in the spectrum of  $CH_3CD_2OH$  (Figure S7B). On the other hand, the isotopic substitution of the  $CH_3$  reveals a part of the overlapping contributions, as observed more clearly in the second derivative spectrum of  $CD_3CH_2OH$  (Figure S7C). This effect is well seen in the calculated spectra (Figure S7C).

The higher frequency NIR region ( $>7000\text{ cm}^{-1}$ ) is also very sensitive to the isotopic effect. A weak absorption from the higher order overtones and combination bands creates difficulties in the analysis

of this region. The deuteration of the OH group significantly reduces the number of the bands as a result of red-shift of the combination bands. The simulated spectra confirmed the high isotopic purity of the samples, except of  $\text{CD}_3\text{CD}_2\text{OD}$  which shows the  $2\nu\text{OH}$  peak near  $7100\text{ cm}^{-1}$  in the experimental spectrum (Figure 6B). This is in contrast to previously studied methanol, in which various non-uniform substitutions have been identified [41]. Contrary to  $-\text{CX}$  bonds, the H or D atoms in  $-\text{OX}$  bonds are labile, therefore, the OD group tends to exchange into the OH even by exposition of the deuterated alcohol to air. Since this band has a high absorptivity, therefore even small impurities due to the OH appear in NIR spectrum as a clear band at  $7100\text{ cm}^{-1}$ . In contrast, no  $-\text{CH}$  bands are observed in the spectrum of  $\text{CD}_3\text{CD}_2\text{OD}$  (Figure 6B). NIR spectroscopy is particularly sensitive and selective for the isotopic effect, although the theoretical calculations are necessary for proper spectra interpretation. The spectral manifestations of the OH group in OD derivatives are obscured by ternary combinations from the CH vibrations that appear in the same region. For example, the  $\delta_{\text{as}}'\text{CH}_3 + \nu_s\text{CH}_2 + \nu_{\text{as}}\text{CH}_2$  bands in  $\text{CH}_3\text{CH}_2\text{OD}$  (Figure 5B), and  $\delta_{\text{sciss}}\text{CH}_2 + \nu_s\text{CH}_2 + \nu_{\text{as}}\text{CH}_2$  bands in  $\text{CD}_3\text{CH}_2\text{OD}$  (Figure 6D) are observed.

One can speculate that the isotopic substitution and conformational isomerism lead to convoluted spectral changes. This phenomenon will be a subject of our next paper (in preparation).

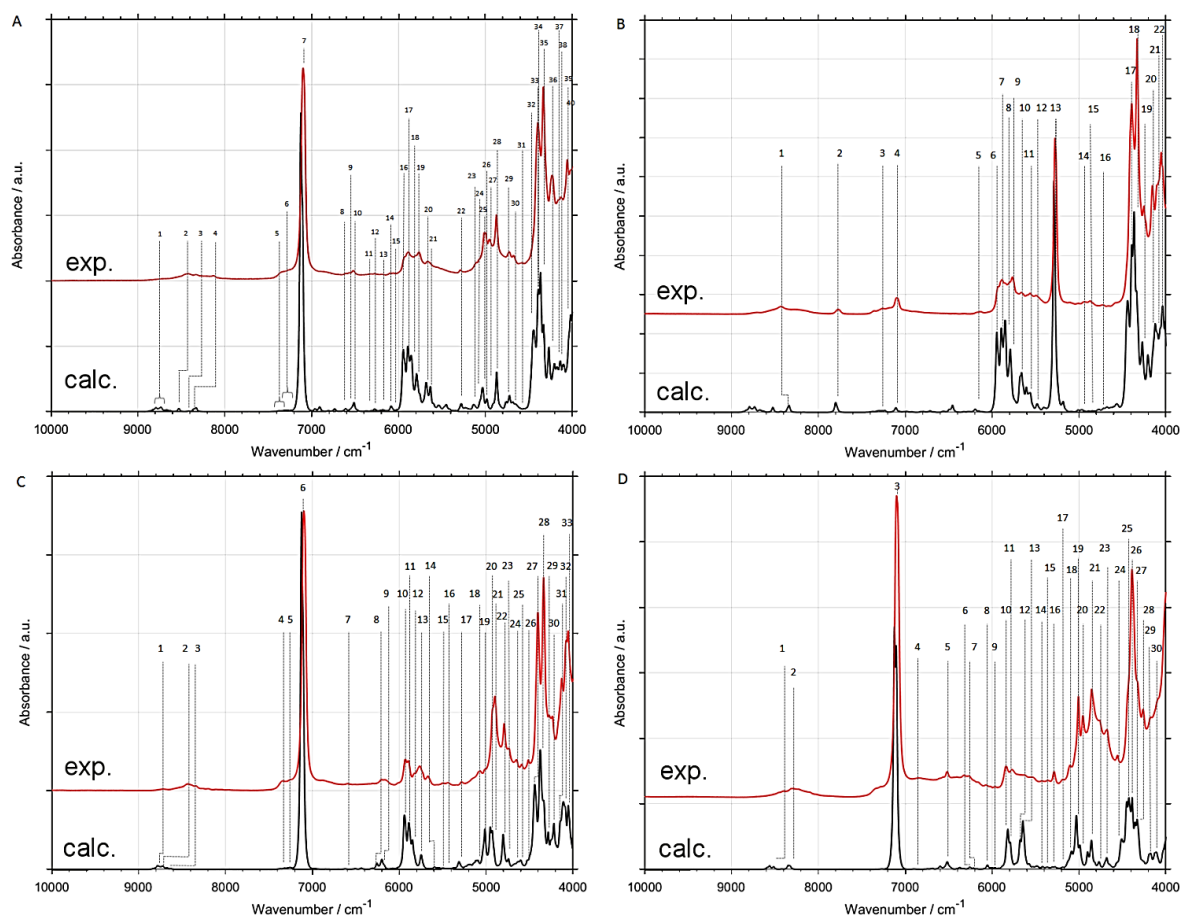


**Figure 5.** Band assignments in NIR spectra of deuterated ethanols based on GVPT2//B2PLYP-GD3BJ/def2-TZVP//CPCM calculations. (A)  $\text{CH}_3\text{CH}_2\text{OH}$ ; (B)  $\text{CH}_3\text{CH}_2\text{OD}$ ; (C)  $\text{CH}_3\text{CD}_2\text{OH}$ ; (D)  $\text{CD}_3\text{CH}_2\text{OH}$ . Band numbering corresponds to that presented in Tables 2–5.

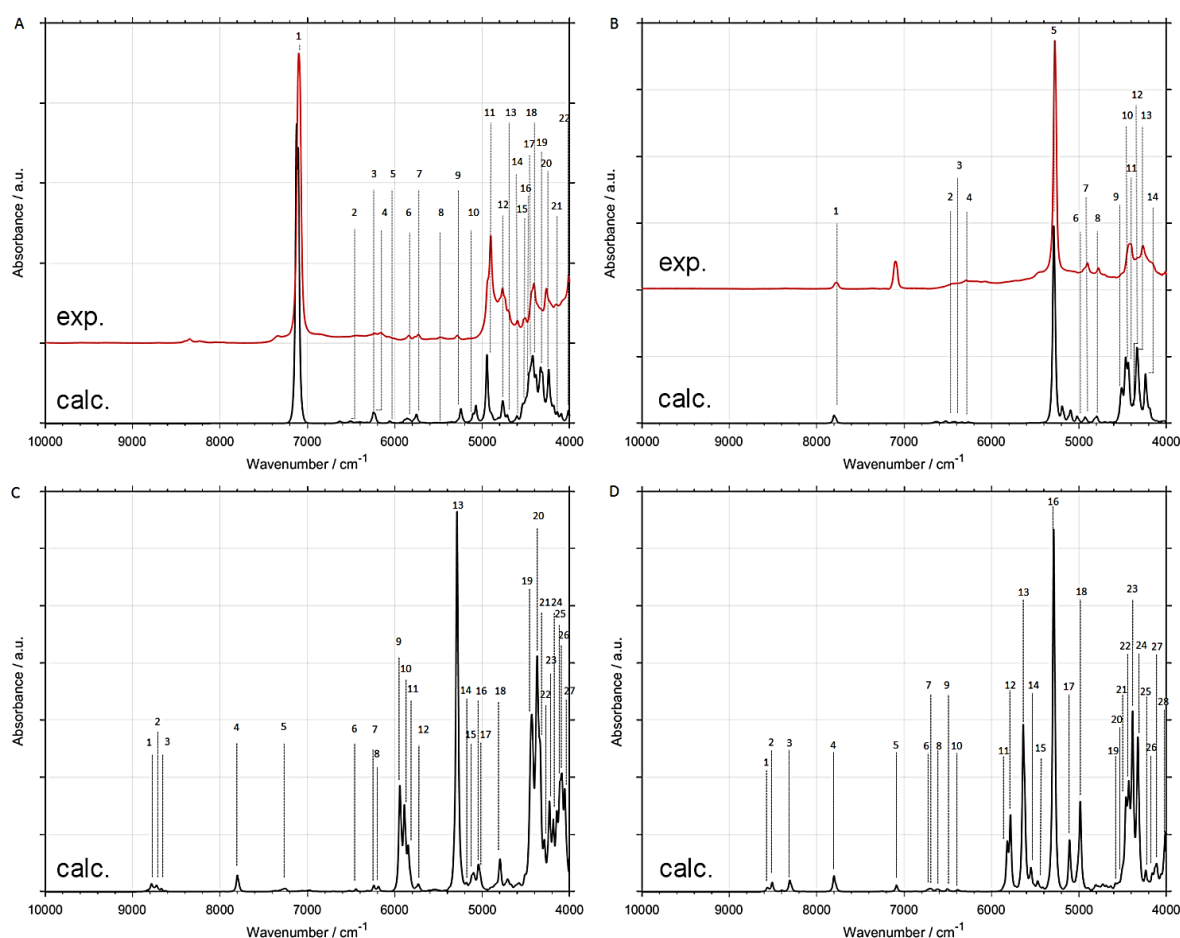


**Figure 6.** Band assignments in NIR spectra of deuterated ethanols based on GVPT2//B2PLYP-GD3BJ/def2-TZVP//CPCM calculations. (A)  $\text{CD}_3\text{CD}_2\text{OH}$ ; (B)  $\text{CD}_3\text{CD}_2\text{OD}$ ; (C)  $\text{CH}_3\text{CD}_2\text{OD}$ ; (D)  $\text{CD}_3\text{CH}_2\text{OD}$ . Band numbering corresponds to that presented in Tables 6–9.

**Table 2.** Band assignments in NIR spectra of  $\text{CH}_3\text{CH}_2\text{OH}$  based on GVPT2//B2PLYP-GD3BJ/def2-TZVP//CPCM calculations. Band numbering corresponds to that presented in Figure 5A.

Peak Number	$\nu_{\text{Exp}}$	$\nu_{\text{Calc}}$	Assignment (Major Contribution)
1	8718.0	8739	$2\nu_{\text{as}}\text{CH}_2 + \nu_{\text{as}}\text{CH}_3$
2	8430.0	8526	$3\nu_{\text{as}}\text{CH}_2$
3	8329.0	8416	$3\nu_{\text{s}}\text{CH}_2$
4	8131.0	8329	$2\nu_{\text{s}}\text{CH}_2 + \nu_{\text{as}}\text{CH}_2$ $\delta_{\text{s}}\text{CH}_3 + \nu_{\text{as}}\text{CH}_3 + \nu_{\text{as}}'\text{CH}_3$
5	7400–7300	7400–7300	$[\delta_{\text{as}}'\text{CH}_3, \delta_{\text{as}}\text{CH}_3] + \nu_{\text{as}}\text{CH}_3 + \nu_{\text{as}}'\text{CH}_3$ $\delta_{\text{sciss}}\text{CH}_2 + \nu_{\text{as}}\text{CH}_2 + \nu_{\text{as}}'\text{CH}_3$ $[\delta_{\text{rock}}\text{CH}_2, \delta_{\text{rock}}\text{CH}_3] + \nu_{\text{as}}\text{CH}_2 + \nu_{\text{OH}}$ $\delta_{\text{twist}}\text{CH}_2 + \nu_{\text{as}}\text{CH}_3 + \nu_{\text{as}}'\text{CH}_3$
6	7300–7200	7300–7200	$\delta_{\text{s}}\text{CH}_3 + \nu_{\text{s}}\text{CH}_3 + \nu_{\text{as}}'\text{CH}_3$ $[\delta_{\text{as}}\text{CH}_3, \delta_{\text{as}}'\text{CH}_3] + \nu_{\text{s}}\text{CH}_3 + \nu_{\text{as}}\text{CH}_3$ $[\delta_{\text{as}}\text{CH}_3, \delta_{\text{as}}'\text{CH}_3] + \nu_{\text{s}}\text{CH}_3 + \nu_{\text{as}}'\text{CH}_3$
7	7099.0	7125	$2\nu_{\text{OH}}$
8	6610.0	6609	$\nu_{\text{s}}\text{CH}_3 + \nu_{\text{OH}}$
9	6565.0	6540	$2\delta_{\text{as}}\text{CH}_3 + \nu_{\text{OH}}$
10	6520.4	6513	$\nu_{\text{s}}\text{CH}_2 + \nu_{\text{OH}}$
11	6331.0	6314	$2\delta_{\text{twist}}\text{CH}_2 + \nu_{\text{OH}}$
12	6271.8	6275	$\delta_{\text{ip}}\text{COH} + \delta_{\text{wagg}}\text{CH}_2 + \nu_{\text{OH}}$
13	6193.0	6178	$[\tau_{\text{CC}}, \delta_{\text{oop}}\text{COH}] + \nu_{\text{as}}\text{CH}_3 + \nu_{\text{as}}'\text{CH}_3$

Table 2. Cont.

Peak Number	$\nu_{Exp}$	$\nu_{Calc}$	Assignment (Major Contribution)
14	6063.0	6085	$2\delta_{ip}COH + \nu OH$
15	6051.0	6021	$[\nu CC, \delta_{ip}COH] + \delta_{twist}CH_2 + \nu OH$
16	5936.0	5948	$2\nu_{as'}CH_3, \nu_{as}CH_3 + \nu_{as'}CH_3$
17	5886.1	5889	$2\delta_{as'}CH_3 + \nu OH$
18	5809.0	5846	$[\delta_{as}CH_3, \delta_{as'}CH_3] + \delta_{sciss}CH_2 + \nu_{as}CH_2$
19	5765.7	5790	$2\nu_{as}CH_2$
20	5665.1	5681	$2\nu_sCH_2; 2\nu_sCH_3 + \delta_sCH_3$
21	5634.0	5632	$\delta_{ip}COH + \delta_{wagg}CH_2 + \nu_sCH_3$
22	5287.6	5277	$\delta_{ip}OH + \delta_{CCO} + \nu OH$
23	5111.0	5128	$\delta_{sciss}CH_2 + \nu OH$
24	5071.0	5118	$[\delta_{as}CH_3, \delta_{as'}CH_3] + \nu OH$
25	5013.8		
26	4996.2	5029	$[\delta_{wagg}CH_2, \delta_sCH_3] + \nu OH$
27	4954.2	4979	$[\delta_{twist}CH_2, \delta_{ip}COH, \delta_{wagg}CH_2] + \nu OH$
28	4873.0	4868	$\delta_{ip}COH + \nu OH$
29	4724.3	4763	$\delta_sCH_3 + 2[\delta_{as}CH_3, \delta_{as'}CH_3]$
30	4677.0	4726	$[\nu CO, \delta_{rock'}CH_3] + \nu OH$
31	4582.9	4648	$[\delta_{oop}COH, \tau CC] + \delta_{as'}CH_3 + \nu_sCH_3$
32	4454.0	4450	$3\delta_{sciss}CH_2$
33	4409.0	4396	$\delta_{sciss}CH_2 + \nu_{as}CH_2$
34	4394.8	4366	$\delta_sCH_3 + \nu_{as'}CH_3$
35	4333.5	4331	$[\delta_{oop}COH, \tau CC] + \nu OH$
36	4232.6	4269	$\delta_{twist}CH_2 + \nu_{as'}CH_3$
37	4162.0	4177	$\delta_{ip}COH + \nu_sCH_2$
38	4131.7	4137	$\delta_{twist}CH_2 + \nu_sCH_2$
39	4057.4	4020	$[\delta_{rock}CH_2, \delta_{rock}CH_3] + \nu_sCH_2$
40	4024.0	3997	$[\nu CO, \delta_{rock'}CH_3] + \nu_{as}CH_2$

Table 3. Band assignments in NIR spectra of CH<sub>3</sub>CH<sub>2</sub>OD based on GVPT2//B2PLYP-GD3BJ/def2-TZVP//CPCM calculations. Band numbering corresponds to that presented in Figure 5B.

Peak Number	$\nu_{exp}$	$\nu_{calc}$	Assignment (Major Contribution)
1	8428.0	8334	$2\nu_sCH_2 + \nu_{as}CH_2$
2	7777.5	7796	$3\nu OD$
3	7260.0	7227	$\delta_{twist}CH_2 + \nu_{as}CH_3 + \nu_{as'}CH_3$
4	7099.1	7112	$\delta_{as'}CH_3 + \nu_sCH_2 + \nu_{as}CH_2$
5	6133.4	6200	$\tau CC + \nu_{as}CH_3 + \nu_{as'}CH_3$
6	5935.0	5946	$2\nu_{as'}CH_3$
7	5885.2	5895	$2\nu_{as}CH_3$
8	5850.0	5847	$[\delta_{as}CH_3, \delta_{as'}CH_3] + \delta_{sciss}CH_2 + \nu_{as}CH_2$
9	5765.6	5788	$2\nu_{as}CH_2$
10	5665.7	5669	$2\delta_{wagg}CH_2 + \nu_sCH_2$
11	5564.3	5559	$\nu OD + \nu_sCH_2$
12	5494.3	5498	$\nu_{as}CH_2 + \delta_{twist}CH_2 + \delta_{wagg}CH_2$
13	5277.1	5289	$2\nu OD$
14	4947.0	4963	$[\delta_{rock}CH_2, \delta_{rock}CH_3] + \delta_{twist}CH_2 + \nu_sCH_2$
15	4873.0	4846	$[\delta_{rock}CH_2, \delta_{rock}CH_3] + [\delta_{rock}CH_2, \delta_{rock}CH_3] + \nu_sCH_2$
16	4720.8	4717	$[\nu CO, \delta_{rock'}CH_3, \delta_{ip}COD] + [\delta_{rock'}CH_3, \delta_{ip}COD, \delta_{sciss}CH_2CO] + \nu OD$
17	4393.7	4397	$\delta_{sciss}CH_2 + \nu_{as}CH_2$
18	4331.8	4364	$[\delta_sCH_3, \delta_{wagg}CH_2] + \nu_{as}CH_3$
19	4253.4	4275	$\delta_{twist}CH_2 + \nu_{as'}CH_3$
20	4155.1	4127	$[\delta_{rock'}CH_3, \delta_{ip}COD, \delta_{sciss}CH_2CO] + \nu_{as}CH_3$
21	4105.0	4063	$[\delta_{rock'}CH_3, \delta_{ip}COD, \delta_{sciss}CH_2CO] + \nu_sCH_3$
22	4054.1	4037	$[\delta_{rock}CH_2, \delta_{rock}CH_3] + \delta_sCH_2$

**Table 4.** Band assignments in NIR spectra of CH<sub>3</sub>CD<sub>2</sub>OH based on GVPT2//B2PLYP-GD3BJ/def2-TZVP//CPCM calculations. Band numbering corresponds to that presented in Figure 5C.

Peak Number	$\nu_{\text{exp}}$	$\nu_{\text{calc}}$	Assignment (Major Contribution)
1	8717.0	8788	$3\nu_{\text{as}}\text{CH}_3$
2	8434.1	8728	$\nu_{\text{s}}\text{CH}_3 + \nu_{\text{as}}\text{CH}_3 + \nu_{\text{as}}'\text{CH}_3$
3	8337.0	8665	$2\nu_{\text{s}}\text{CH}_3 + \nu_{\text{as}}\text{CH}_3$
4	7345.0	7324	$[\delta_{\text{rock}}\text{CD}_2, \delta_{\text{twist}}\text{CD}_2] + \nu_{\text{as}}'\text{CH}_3 + \nu_{\text{OH}}$
5	7251.0	7255	$[\delta_{\text{as}}\text{CH}_3, \delta_{\text{as}}'\text{CH}_3] + \nu_{\text{s}}\text{CH}_3 + \nu_{\text{as}}\text{CH}_3$
6	7098.2	7126	$2\nu_{\text{OH}}$
7	6590.4	6618	$\nu_{\text{as}}'\text{CH}_3 + \nu_{\text{OH}}$
8	6205.8	6257	$2\delta_{\text{ip}}\text{COH} + \nu_{\text{OH}}$
9	6158.0	6198	$2\delta_{\text{ip}}\text{COH} + \nu_{\text{OH}}$
10	5929.9	5943	$2\nu_{\text{as}}\text{CH}_3$
11	5895.4	5892	$2\nu_{\text{as}}'\text{CH}_3$
12	5828.0	5844	$\nu_{\text{s}}\text{CH}_3 + \nu_{\text{as}}'\text{CH}_3$
13	5763.8	5744	$\nu_{\text{s}}\text{CD}_2 + \nu_{\text{OH}}$
14	5669.1	5595	$\nu_{\text{s}}\text{CH}_3 + 2\nu_{\text{as}}\text{CH}_3$
15	5449.0	5496	$\delta_{\text{rock}}\text{CH}_3 + \delta_{\text{s}}\text{CH}_3 + \nu_{\text{as}}'\text{CH}_3$
16	5439.4	5449	$\delta_{\text{sciss}}\text{CD}_2\text{CO} + 2\nu_{\text{as}}\text{CH}_3$
17	5282.0	5309	$\nu_{\text{as}}\text{CD}_2 + 2[\delta_{\text{as}}\text{CH}_3, \delta_{\text{as}}'\text{CH}_3]$
18	5070.1	5094	$\nu_{\text{s}}\text{CD}_2 + \nu_{\text{as}}\text{CH}_3$
19	5017.0	5018	$[\tau_{\text{CC}}, \delta_{\text{oop}}\text{COH}] + 2[\delta_{\text{as}}\text{CH}_3, \delta_{\text{as}}'\text{CH}_3]$
20	4927.0	4954	$\delta_{\text{ip}}\text{COH} + \nu_{\text{OH}}$
21	4898.3	4930	$\delta_{\text{ip}}\text{COH} + \nu_{\text{OH}}$
22	4792.1	4806	$[\nu_{\text{CO}}, \delta_{\text{wagg}}\text{CD}_2] + \nu_{\text{OH}}$
23	4737.2	4744	$\delta_{\text{sciss}}\text{CD}_2 + \nu_{\text{OH}}$
24	4650.2	4641	$[\nu_{\text{CC}}, \delta_{\text{rock}}'\text{CH}_3] + \nu_{\text{OH}}$
25	4591.7	4600	$[\nu_{\text{CO}}, \delta_{\text{wagg}}\text{CD}_2] + \nu_{\text{OH}}$
26	4513.3	4525	$\delta_{\text{ip}}\text{COH} + \nu_{\text{OH}}$
27	4404.6	4437	$[\delta_{\text{as}}\text{CH}_3, \delta_{\text{as}}'\text{CH}_3] + \nu_{\text{as}}'\text{CH}_3$
28	4338.0	4373	$\delta_{\text{s}}\text{CH}_3 + \nu_{\text{as}}'\text{CH}_3$
29	4275.7	4285	$\delta_{\text{ip}}\text{COH} + \nu_{\text{as}}\text{CH}_3$
30	4238.1	4218	$\nu_{\text{s}}\text{CD}_2 + \nu_{\text{as}}\text{CD}_2$
31	4129.6	4147	$[\nu_{\text{CO}}, \delta_{\text{wagg}}\text{CD}_2] + \nu_{\text{as}}'\text{CH}_3$
32	4079.7	4117	$\delta_{\text{rock}}\text{CH}_3 + \nu_{\text{as}}\text{CH}_3$
33	4056.2	4052	$\delta_{\text{rock}}\text{CH}_3 + \nu_{\text{s}}\text{CH}_3, \delta_{\text{sciss}}\text{CD}_2\text{CO} + \nu_{\text{OH}}$

**Table 5.** Band assignments in NIR spectra of CD<sub>3</sub>CH<sub>2</sub>OH based on GVPT2//B2PLYP-GD3BJ/def2-TZVP//CPCM calculations. Band numbering corresponds to that presented in Figure 5D.

Peak Number	$\nu_{\text{exp}}$	$\nu_{\text{calc}}$	Assignment (Major Contribution)
1	8405.0	8511	$3\nu_{\text{as}}\text{CH}_2$
2	8307.6	8323	$2\nu_{\text{s}}\text{CH}_2 + \nu_{\text{as}}\text{CH}_2$
3	7098.5	7124 (f) 7100 (g)	$2\nu_{\text{OH}}$
4	6841.1	6897	$[\nu_{\text{CO}}, \delta_{\text{as}}'\text{CD}_3] + \nu_{\text{s}}\text{CH}_2 + \nu_{\text{as}}\text{CH}_2$
5	6517.6	6510	$\nu_{\text{s}}\text{CH}_2 + \nu_{\text{OH}}$
6	6324.0	6261	$[\delta_{\text{ip}}\text{COH}, \delta_{\text{twist}}\text{CH}_2] + \delta_{\text{wagg}}\text{CH}_2 + \nu_{\text{OH}}$
7	6268.0	6111	$[\delta_{\text{rock}}'\text{CD}_3, \nu_{\text{CC}}] + \nu_{\text{as}}'\text{CD}_3 + \nu_{\text{OH}}$
8	6070.4	6059	$2[\delta_{\text{ip}}\text{COH}, \delta_{\text{twist}}\text{CH}_2] + \nu_{\text{OH}}$
9	5966.3	5966	$[\delta_{\text{s}}\text{CD}_3, \nu_{\text{CC}}] + \delta_{\text{wagg}}\text{CH}_2 + \nu_{\text{OH}}$
10	5839.1	5825	$2\nu_{\text{as}}\text{CH}_2$
11	5772.1	5793	$2\nu_{\text{as}}\text{CH}_2$
12	5628.0	5686	$2\nu_{\text{s}}\text{CH}_2$
13	5533.0	5641	$2\nu_{\text{s}}\text{CH}_2$
14	5427.9	5419	$2\delta_{\text{twist}}\text{CH}_2 + \nu_{\text{as}}\text{CH}_2$
15	5358.0	5367	$[\nu_{\text{CO}}, \delta_{\text{as}}'\text{CD}_3] + \nu_{\text{s}}\text{CD}_3 + \nu_{\text{as}}'\text{CD}_3$
16	5286.8	5287	$\delta_{\text{s}}\text{CD}_3 + \delta_{\text{twist}}\text{CH}_2 + \nu_{\text{as}}\text{CH}_2$

Table 5. Cont.

Peak Number	$\nu_{\text{exp}}$	$\nu_{\text{calc}}$	Assignment (Major Contribution)
17	5190.0	5188	$2[\delta_s\text{CD}_3, \nu\text{CC}] + \nu_s\text{CH}_2$
18	5102.7	5084	$\delta_{\text{oop}}\text{COH} + 2\delta_{\text{wagg}}\text{CH}_2$
19	5007.1	5028	$\delta_{\text{wagg}}\text{CH}_2 + \nu\text{OH}$
20	4955.8	4987	$[\delta_{\text{twist}}\text{CH}_2, \delta_{\text{ip}}\text{COH}, \delta_{\text{wagg}}\text{CH}_2] + \nu\text{OH}$
21	4853.8	4853	$[\delta_{\text{ip}}\text{COH}, \delta_{\text{twist}}\text{CH}_2] + \nu\text{OH}$
22	4764.7	4768	$[\delta_s\text{CD}_3, \nu\text{CC}] + \nu\text{OH}$
23	4676.7	4676	$\nu\text{CO} + \nu\text{OH}$
24	4558.4	4511	$\delta_{\text{as}}'\text{CD}_3 + [\delta_{\text{twist}}\text{CH}_2, \delta_{\text{ip}}\text{COH}] + \nu_{\text{as}}'\text{CD}_3$
25	4443.0	4429	$\delta_{\text{sciss}}\text{CH}_2 + \nu_{\text{as}}\text{CH}_2$
26	4390.5	4390	$\delta_{\text{sciss}}\text{CH}_2 + \nu_{\text{as}}\text{CH}_2$
27	4329.0	4356	$\delta_{\text{sciss}}\text{CH}_2 + \nu_s\text{CH}_2$
28	4263.8	4332	$\delta_{\text{sciss}}\text{CH}_2 + \nu_s\text{CH}_2$
29	4174.6	4180	$2[\delta_{\text{twist}}\text{CH}_2, \delta_{\text{ip}}\text{COH}, \delta_{\text{wagg}}\text{CH}_2] + \delta_{\text{sciss}}\text{CH}_2$
30	4100.0	4107	$\tau\text{CC} + \delta_{\text{oop}}\text{COH} + \nu\text{OH}$

Table 6. Band assignments in NIR spectra of  $\text{CD}_3\text{CD}_2\text{OH}$  based on GVPT2//B2PLYP-GD3BJ/def2-TZVP//CPCM calculations. Band numbering corresponds to that presented in Figure 6A.

Peak Number	$\nu_{\text{exp}}$	$\nu_{\text{calc}}$	Assignment (Major Contribution)
1	7099.0	7126 (f) 7102 (g)	$2\nu\text{OH}$
2	6444.0	6495	$\nu_s\text{CD}_2 + [\nu_{\text{as}}\text{CD}_2, \nu_{\text{as}}\text{CD}_3] + [\nu_{\text{as}}'\text{CD}_3, \nu_{\text{as}}\text{CD}_2]$
3	6232.1	6244	$2\delta_{\text{ip}}\text{COH} + \nu\text{OH}$
4	6162.9	6224	$2[\nu\text{CC}, \delta_{\text{wagg}}\text{CD}_2] + \nu\text{OH}$
5	6063.0	6059	$[\delta_{\text{sciss}}\text{CD}_2, \nu\text{CO}] + [\nu\text{CC}, \delta_{\text{wagg}}\text{CD}_2] + \nu\text{OH}$
6	5838.3	5861	$[\nu_{\text{as}}\text{CD}_2, \nu_{\text{as}}\text{CD}_3] + \nu\text{OH}$
7	5732.3	5746	$[\delta_{\text{rock}}\text{CD}_2, \delta_{\text{rock}}\text{CD}_3] + [\delta_s\text{CD}_3, \delta_{\text{wagg}}\text{CD}_2] + \nu\text{OH}$
8	5478.7	5488	$[\nu\text{CC}, \delta_{\text{wagg}}\text{CD}_2] + \nu_s\text{CD}_3 + [\nu_{\text{as}}\text{CD}_2, \nu_{\text{as}}\text{CD}_3]$
9	5285.8	5247	$\nu_s\text{CD}_3 + \nu_{\text{as}}\text{CD}_2 + \nu\text{CO}$
10	5160.0	5103	$[\delta_{\text{twist}}\text{CD}_2, \delta_{\text{rock}}\text{CD}_3, \delta_{\text{rock}}\text{CD}_2] + 2[\nu\text{CC}, \delta_{\text{wagg}}\text{CD}_2]$
11	4903.7	4947	$\delta_{\text{ip}}\text{COH} + \nu\text{OH}$
12	4769.2	4766	$[\delta_{\text{sciss}}\text{CD}_2, \nu\text{CO}] + \nu\text{OH}$
13	4701.4	4714	$[\delta_{\text{as}}'\text{CD}_3, \delta_{\text{as}}\text{CD}_3] + \nu\text{OH}$
14	4598.4	4604	$[\nu\text{CO}, \delta_{\text{wagg}}\text{CD}_2] + \nu\text{OH}$
15	4525.0	4539	$[\delta_{\text{twist}}\text{CD}_2, \delta_{\text{rock}}\text{CD}_3, \delta_{\text{rock}}\text{CD}_2] + \delta_{\text{ip}}\text{COH} + [\nu_{\text{as}}'\text{CD}_3, \nu_{\text{as}}\text{CD}_2]$
16	4506.9	4499	$2\delta_{\text{sciss}}\text{CD}_2\text{CO} + \nu_{\text{as}}\text{CD}_3$
17	4430.0	4447	$[\nu_{\text{as}}\text{CD}_2, \nu_{\text{as}}\text{CD}_3] + \nu_{\text{as}}\text{CD}_3, 2[\nu_{\text{as}}'\text{CD}_3, \nu_{\text{as}}\text{CD}_2]$
18	4409.6	4420	$[\nu_{\text{as}}\text{CD}_2, \nu_{\text{as}}\text{CD}_3] + [\nu_{\text{as}}'\text{CD}_3, \nu_{\text{as}}\text{CD}_2]$
19	4332.0	4334	$2\nu_{\text{as}}\text{CD}_2$
20	4267.4	4235	$[\nu_s\text{CD}_2, \nu_s\text{CD}_3] + \nu_{\text{as}}\text{CD}_2$
21	4156.8	4140	$2\delta_{\text{oop}}\text{COH} + \nu\text{OH}$
22	4013.0	4012	$\delta_{\text{sciss}}\text{CD}_2\text{CO} + \nu\text{OH}$

Table 7. Band assignments in NIR spectra of  $\text{CD}_3\text{CD}_2\text{OD}$  based on GVPT2//B2PLYP-GD3BJ/def2-TZVP//CPCM calculations. Band numbering corresponds to that presented in Figure 6B.

Peak Number	$\nu_{\text{Exp}}$	$\nu_{\text{Calc}}$	Assignment (Major Contribution)
1	7771.0	7799	$3\nu\text{OD}$
2	6468.0	6525	$\nu_s\text{CD}_3 + [\nu_{\text{as}}'\text{CD}_3, \nu_{\text{as}}\text{CD}_2] + \nu_{\text{as}}\text{CD}_3$
3	6450.0	6447	$3\nu_{\text{as}}\text{CD}_2$
4	6290.1	6267	$2\nu_s\text{CD}_2 + \nu_{\text{as}}\text{CD}_2$
5	5276.0	5289	$2\nu\text{OD}$
6	4948.0	5020	$[\nu\text{CO}, \delta_{\text{twist}}\text{CD}_2] + 2[\delta_{\text{sciss}}\text{CD}_2, \nu\text{CO}]$
7	4902.2	4929	$[\delta_{\text{twist}}\text{CD}_2, \delta_{\text{rock}}\text{CD}_2] + 2[\delta_{\text{sciss}}\text{CD}_2, \nu\text{CO}]$
8	4779.2	4795	$\nu_s\text{CD}_2 + \nu\text{OD}$

Table 7. Cont.

Peak Number	$\nu_{Exp}$	$\nu_{Calc}$	Assignment (Major Contribution)
9	4509.0	4510	$[\delta_{as}CD_3, \delta_{as}'CD_3] + [\nu_{CC}, \delta_{wagg}CD_2] + \nu_{as}CD_3$
10	4437.4	4465	$2\nu_{as}'CD_3, \nu_{as}CD_3 + \nu_{as}'CD_3$
11	4409.3	4434	$2\nu_{as}CD_3, \nu_{as}CD_2 + \nu_{as}'CD_3$
12	4325.2	4381	$2[\delta_{sciss}CD_2, \nu_{CO}] + \nu_sCD_3$
13	4269.5	4337	$2\nu_{as}CD_2$
14	4170.2	4241	$[\nu_sCD_2, \nu_sCD_3] + \nu_{as}CD_2$

Table 8. Band assignments in NIR spectra of  $CH_3CD_2OD$  based on GVPT2//B2PLYP-GD3BJ/def2-TZVP//CPCM calculations. Band numbering corresponds to that presented Figure 6C.

Peak Number	$\nu_{Calc}$	Assignment (Major Contribution)
1	8781	$3\nu_{as}'CH_3$
2	8722	$\nu_sCH_3 + \nu_{as}CH_3 + \nu_{as}'CH_3$
3	8666	$2\nu_sCH_3 + \nu_{as}CH_3, 2\nu_sCH_3 + \nu_{as}'CH_3$
4	7802	$3\nu_{OD}$
5	7257	$[\delta_{as}CH_3, \delta_{as}'CH_3] + \nu_sCH_3 + \nu_{as}CH_3$
6	6445	$3\nu_{as}CD_2$
7	6188	$\tau_{CC} + \nu_{as}CH_3 + \nu_{as}'CH_3$
8	5943	$2\nu_{as}CH_3, \nu_{as}CH_3 + \nu_{as}'CH_3$
9	5890	$2[\delta_{as}'CH_3, \delta_{as}CH_3] + \nu_{as}'CH_3, 2\nu_{as}'CH_3$
10	5845	$\nu_sCH_3 + \nu_{as}CH_3$
11	5728	$2\delta_sCH_3 + \nu_{as}CH_3$
12	5288	$2\nu_{OD}$
13	5182	$\nu_{as}CD_2 + \nu_{as}'CH_3$
14	5120	$\nu_{as}CD_2 + \nu_sCH_3$
15	5097	$\nu_sCD_2 + \nu_{as}CH_3$
16	5046	$\tau_{CC} + 2[\delta_{as}CH_3, \delta_{as}'CH_3]$
17	4796	$\delta_{oop}COD + 2[\delta_{as}'CH_3, \delta_{as}CH_3]$
18	4434	$\tau_{CC} + [\delta_{wagg}CD_2, \nu_{CC}] + \nu_{as}'CH_3$
19	4372	$\delta_sCH_3 + \nu_{as}CH_3, \delta_sCH_3 + \nu_{as}'CH_3$
20	4341	$2\nu_{as}CD_2$
21	4289	$\tau_{CC} + \delta_{sciss}CD_2 + [\delta_{sciss}CD_2, \nu_{CO}]$
22	4233	$\nu_sCD_2 + \nu_{as}CD_2$
23	4190	$2\nu_sCD_2, [\delta_{wagg}CD_2, \nu_{CC}] + \nu_{as}CH_3$
24	4149	$[\delta_{sciss}CD_2, \nu_{CO}] + \nu_{as}CH_3, [\delta_{sciss}CD_2, \nu_{CO}] + \nu_{as}'CH_3$
25	4113	$\delta_{rock}CH_3 + \nu_{as}'CH_3$
26	4089	$[\delta_{sciss}CD_2, \nu_{CO}] + \nu_sCH_3$
27	4056	$\delta_{rock}CH_3 + \nu_sCH_3$

Table 9. Band assignments in NIR spectra of  $CD_3CH_2OD$  based on GVPT2//B2PLYP-GD3BJ/def2-TZVP//CPCM calculations. Band numbering corresponds to that presented Figure 6D.

Peak Number	$\nu_{calc}$	Assignment (Major Contribution)
1	8560	$3\nu_{as}CH_2, 2\nu_sCH_2 + \nu_{as}CH_2$
2	8508	$3\nu_{as}CH_2$
3	8305	$2\nu_sCH_2 + \nu_{as}CH_2$
4	7802	$3\nu_{OD}$
5	7088	$\delta_{sciss}CH_2 + \nu_sCH_2 + \nu_{as}CH_2$
6	6736	$\delta_{rock}CH_2 + \nu_sCH_2 + \nu_{as}CH_2$
7	6706	$[\nu_{CO}, \delta_{as}'CD_3] + \nu_sCH_2 + \nu_{as}CH_2$
8	6614	$3\nu_{as}'CD_3$
9	6505	$\nu_sCD_3 + \nu_{as}CD_3 + \nu_{as}'CD_3$
10	6382	$2\nu_sCD_3 + \nu_{as}CD_3, 2\nu_sCD_3 + \nu_{as}'CD_3$
11	5821	$[\delta_{oop}COD, \tau_{CC}] + \nu_{as}CH_2 + \nu_sCH_2$
12	5785	$2\nu_{as}CH_2, \delta_{wagg}CH_2 + \delta_{sciss}CH_2 + \nu_{as}CH_2$

Table 9. Cont.

Peak Number	$\nu_{\text{calc}}$	Assignment (Major Contribution)
13	5638	$2\nu_s\text{CH}_2, \nu_s\text{CH}_2 + \nu_{\text{as}}\text{CH}_2$
14	5547	$\nu\text{OD} + \nu_s\text{CH}_2$
15	5473	$\delta_{\text{rock}}\text{CH}_2 + \delta_{\text{sciss}}\text{CH}_2 + \nu_{\text{as}}\text{CH}_2$
16	5288	$2\nu\text{OD}$
17	5106	$[\tau\text{CC}, \delta_{\text{oop}}\text{COD}] + 2\delta_{\text{wagg}}\text{CH}_2$
18	4986	$2[\nu\text{CC}, \delta_s\text{CD}_3] + \nu\text{OD}$
19	4585	$\delta_{\text{rock}}'\text{CD}_3 + 2\delta_{\text{wagg}}\text{CH}_2$
20	4503	$[\tau\text{CC}, \delta_{\text{oop}}\text{COD}] + \delta_{\text{wagg}}\text{CH}_2 + \nu_{\text{as}}\text{CH}_2$
21	4459	$2\nu_{\text{as}}\text{CD}_3$
22	4431	$[\delta_{\text{as}}'\text{CD}_3, \nu\text{CO}] + [\nu\text{CC}, \delta_s\text{CD}_3] + \nu_{\text{as}}'\text{CD}_3$
23	4385	$\delta_{\text{sciss}}\text{CH}_2 + \nu_{\text{as}}\text{CH}_2$
24	4324	$2\nu_{\text{as}}'\text{CD}_3, \delta_{\text{sciss}}\text{CH}_2 + \nu_s\text{CH}_2$
25	4237	$\delta_{\text{wagg}}\text{CH}_2 + \nu_s\text{CH}_2$
26	4167	$\delta_{\text{twist}}\text{CH}_2 + \nu_{\text{as}}\text{CH}_2$
27	4112	$\delta_{\text{twist}}\text{CH}_2 + \nu_s\text{CH}_2$
28	4015	$[\delta_{\text{rock}}\text{CD}_3, \delta_{\text{rock}}\text{CH}_2] + \delta_{\text{rock}}\text{CH}_2 + \nu_{\text{as}}'\text{CD}_3$

Another insight, which becomes possible only through theoretical simulation of NIR spectra, is estimation of the relative contributions from different kinds of vibrational transitions (Table 10). As compared with methanol [41], ethanol offers better opportunity to analyze these contributions, because of higher number of isotopomers and more complex NIR spectra. The effect of various kinds of isotopic substitution of the  $\text{CH}_3$ ,  $\text{CH}_2$ , and  $\text{OH}$  groups on NIR spectra may be elucidated. In the  $10,000\text{--}4000\text{ cm}^{-1}$  region two quanta transitions, first overtones ( $2\nu_x$ ) and binary combinations ( $\nu_x + \nu_y$ ), are the most meaningful components of the spectra. In particular, binary combinations from the  $\text{CH}_3$  group have significant contribution—e.g., for  $\text{CH}_3\text{CH}_2\text{OH}$  they are responsible for 47% of NIR intensity—while upon deuteration of the  $\text{CH}_3$  group this contribution decreases to 32.6%. An even more pronounced effect is observed for OD derivatives, the analogous values for  $\text{CH}_3\text{CH}_2\text{OD}$  and  $\text{CD}_3\text{CH}_2\text{OD}$  are 51.2% and 35.5%, respectively. Simultaneously, the isotopic substitution of the methyl group increases the relative intensity of the first overtones, while the intensity of the second overtones remains insignificant. As expected, the importance of the second overtones increases in the upper NIR region ( $10,000\text{--}7500\text{ cm}^{-1}$ ). Interestingly, this trend is not observed for the ternary combinations ( $\nu_x + \nu_y + \nu_z$  and  $2\nu_x + \nu_y$ ), although for OD derivatives the  $2\nu_x + \nu_y$  contribution increases and the  $\nu_x + \nu_y + \nu_z$  contribution decreases upon deuteration of the  $\text{CH}_3$  group. The isotopic substitution of the  $\text{CH}_2$  group provides similar changes, but is noticeably less significant.

As can be seen (Table 10), the region above  $7500\text{ cm}^{-1}$  is contributed only by three and higher quanta transitions. Therefore, in this region the effect of isotopic substitution is even more visible. The deuteration of the  $\text{CH}_3$  group increases the contributions from the second overtones at the expense of  $\nu_x + \nu_y + \nu_z$  combinations, while the contributions from  $2\nu_x + \nu_y$  remain similar. Interestingly, NIR spectrum of  $\text{CD}_3\text{CD}_2\text{OD}$  above  $7500\text{ cm}^{-1}$  includes the second overtones only.

These observations remain in agreement with our previous findings on methanol isotopomers [41]. However, the contributions from the three quanta transitions are more important for ethanol. For  $\text{CH}_3\text{CH}_2\text{OH}$  these transitions involve 25.9% of total intensity ( $10,000\text{--}4000\text{ cm}^{-1}$ ), while for  $\text{CH}_3\text{OH}$  this value was found to be 19.2%. The difference between  $\text{CD}_3\text{OD}$  and  $\text{CD}_3\text{CD}_2\text{OD}$  is even larger (23.5% vs. 36.7%).

**Table 10.** Contributions (in %) from the first and second overtones as well as binary and ternary combinations into NIR spectra of ethanol isotopomers based on GVPT2//B2PLYP-GD3BJ/def2-TZVP//CPCM calculations. <sup>a</sup>

	10,000–4000 cm <sup>-1</sup>				
	2ν <sub>x</sub>	3ν <sub>x</sub>	ν <sub>x</sub> + ν <sub>y</sub>	ν <sub>x</sub> + ν <sub>y</sub> + ν <sub>z</sub>	2ν <sub>x</sub> + ν <sub>y</sub>
CH <sub>3</sub> CH <sub>2</sub> OH	26.1	1.7	47.0	14.3	10.9
CH <sub>3</sub> CH <sub>2</sub> OD	18.0	2.2	51.2	17.4	11.1
CH <sub>3</sub> CD <sub>2</sub> OH	35.8	1.7	41.5	11.8	9.2
CD <sub>3</sub> CH <sub>2</sub> OH	40.9	1.2	32.6	15.1	10.1
CD <sub>3</sub> CD <sub>2</sub> OH	46.0	0.3	23.7	15.8	14.2
CD <sub>3</sub> CD <sub>2</sub> OD	43.1	2.0	19.2	17.8	17.9
CH <sub>3</sub> CD <sub>2</sub> OD	27.9	3.2	44.7	15.0	9.2
CD <sub>3</sub> CH <sub>2</sub> OD	36.0	2.5	35.5	10.8	15.2
	10,000–7500 cm <sup>-1</sup>				
	2ν <sub>x</sub>	3ν <sub>x</sub>	ν <sub>x</sub> + ν <sub>y</sub>	ν <sub>x</sub> + ν <sub>y</sub> + ν <sub>z</sub>	2ν <sub>x</sub> + ν <sub>y</sub>
CH <sub>3</sub> CH <sub>2</sub> OH	0.0	39.7	0.0	22.3	38.0
CH <sub>3</sub> CH <sub>2</sub> OD	0.0	55.5	0.0	15.4	29.1
CH <sub>3</sub> CD <sub>2</sub> OH	0.0	43.9	0.0	30.5	25.6
CD <sub>3</sub> CH <sub>2</sub> OH	0.0	66.9	0.0	1.4	31.7
CD <sub>3</sub> CD <sub>2</sub> OH	0.0	0.0	0.0	43.0	57.0
CD <sub>3</sub> CD <sub>2</sub> OD	0.0	100.0	0.0	0.0	0.0
CH <sub>3</sub> CD <sub>2</sub> OD	0.0	69.9	0.0	16.7	13.4
CD <sub>3</sub> CH <sub>2</sub> OD	0.0	76.3	0.0	0.5	23.2
	7500–4000 cm <sup>-1</sup>				
	2ν <sub>x</sub>	3ν <sub>x</sub>	ν <sub>x</sub> + ν <sub>y</sub>	ν <sub>x</sub> + ν <sub>y</sub> + ν <sub>z</sub>	2ν <sub>x</sub> + ν <sub>y</sub>
CH <sub>3</sub> CH <sub>2</sub> OH	26.5	1.2	47.6	14.2	10.5
CH <sub>3</sub> CH <sub>2</sub> OD	18.4	1.0	52.4	17.5	10.7
CH <sub>3</sub> CD <sub>2</sub> OH	36.0	1.4	41.8	11.7	9.1
CD <sub>3</sub> CH <sub>2</sub> OH	41.4	0.4	33.0	15.3	9.9
CD <sub>3</sub> CD <sub>2</sub> OH	46.0	0.3	23.7	15.8	14.2
CD <sub>3</sub> CD <sub>2</sub> OD	43.7	0.5	19.5	18.0	18.2
CH <sub>3</sub> CD <sub>2</sub> OD	28.4	2.0	45.5	15.0	9.1
CD <sub>3</sub> CH <sub>2</sub> OD	37.0	0.5	36.4	11.1	15.0

<sup>a</sup> The comparison is based on integrated intensity (cm<sup>-1</sup>) summed over simulated bands, convoluted with the use of Cauchy–Gauss product function (details in the text) in relation to the total integrated intensity.

### 3. Experimental and Computational Methods

#### 3.1. Materials and Spectroscopic Measurements

In Table 11 are collected the details on the samples used in this work. The experimental spectrum of CH<sub>3</sub>CH<sub>2</sub>OH was taken from our previous work [29]. All samples were used as received, while solvent (CCl<sub>4</sub>) was distilled and additionally dried using freshly activated molecular sieves (Aldrich, 4A). All ethanols were measured in CCl<sub>4</sub> solution (0.1 mol dm<sup>-3</sup>). NIR spectra were recorded on Thermo Scientific Nicolet iS50 spectrometer using InGaAs detector, with a resolution of 2 cm<sup>-1</sup> (128 scans), in a quartz cells (Hellma QX, Hellma Optik GmbH, Jena, Germany) of 100 mm thicknesses at 298 K (25 °C).

Table 11. Samples used in this study

	Sample	Purity	D Atom Content	Other Remarks
1	CH <sub>3</sub> CH <sub>2</sub> OD	99%	≥99.5%	
2	CH <sub>3</sub> CD <sub>2</sub> OH	99%	98%	
3	CD <sub>3</sub> CH <sub>2</sub> OH	99%	99%	
4	CD <sub>3</sub> CD <sub>2</sub> OH	99%	99.5%	
5	CD <sub>3</sub> CD <sub>2</sub> OD	>99%	≥99.5%	anhydrous
6	CCl <sub>4</sub>	>99%	-	

Samples were purchased from Sigma-Aldrich Chemie GmbH (Taufkirchen, Germany).

### 3.2. Computational Procedures

Our calculations were based on density functional theory (DFT) with double-hybrid B2PLYP density functional [55] (unfrozen core) coupled with Karlsruhe triple- $\zeta$  valence with polarization (def2-TZVP) [56] basis set. Grimme's third formulation of empirical correction for dispersion with Becke-Johnson damping (GD3BJ) was applied [57]. To better reflect solvation of molecules, CCl<sub>4</sub> cavity in solvent reaction field (SCRF) [58] was included at conductor-like polarizable continuum (CPCM) [59] level. Very tight criteria for geometry optimization and 10<sup>-10</sup> convergence criterion in SCF procedure were set. Electron integrals and solving coupled perturbed Hartree-Fock (CPHF) equations were calculated over a superfine grid. The selected method provided good reproduction of NIR spectra of various molecules in CCl<sub>4</sub> solution [19,29,30].

We carried out the anharmonic vibrational analysis at generalized vibrational second-order perturbation theory (GVPT2) [60,61] level. In this approach, the anharmonic frequencies and intensities of the vibrational transitions up to three quanta were obtained. This allows to simulate fundamental, first and second overtones, as well as binary and ternary combination bands. Quantum mechanical calculations were carried out with Gaussian 16 (A.03) [62]. One of the major features implemented in GVPT2 approach is the automatic treatment of tight vibrational degenerations, i.e., resonances [63]. In this work the search for resonances included Fermi (i.e., 1-2) of type I ( $\omega_i \approx 2\omega_j$ ) and type II ( $\omega_i \approx \omega_j + \omega_k$ ), and Darling–Dennison (i.e., 2-2, 1-1, and 1-3) resonances. All possible resonant terms within search thresholds were included in the variational treatment. The resonance search thresholds (respectively, maximum frequency difference and minimum difference PT2 vs. variational treatment; in cm<sup>-1</sup>) were: 200 and 1 (for the search of 1–2 resonances), 100 and 10 (for 2-2, 1-1, and 1-3).

To display the simulated spectra we applied a four-parameter Cauchy–Gauss (Lorentz–Gauss) product function [20]. The theoretical bands were modelled with  $a_2$  and  $a_4$  parameters equal to 0.055 and 0.015, resulting with full-width at half-height (FWHH) of 25 cm<sup>-1</sup>. Exception was made for better agreement with the weaker and broader experimental bands, which are presented in Figures 3 and 4. In this case the values were 0.075, 0.015, and 35 cm<sup>-1</sup>, respectively. The final theoretical spectra were obtained by combining the spectra of *trans* and *gauche* conformers, mixed in accordance with the calculated abundances of each form [64]. The relative abundances of the *gauche* ( $n_g$ ) and *trans* ( $n_t$ ) conformers were determined as following equation [65].

$$\frac{n_g}{n_t} = \frac{A_t}{A_g} e^{\frac{-\Delta G^{298}}{RT}}$$

where Gibbs free energy ( $\Delta G$ ) corresponds to the value calculated at 298 K corrected by anharmonic (VPT2) zero-point energy (ZPE);  $A_t$  and  $A_g$  are the degeneracy prefactors of the Boltzmann term for the *gauche* (1) and *trans* (2) conformers.

The band assignments were aided by calculations of potential energy distributions (PEDs). PEDs were obtained with Gar2Ped software [66], using natural internal coordinate system defined in accordance with Pulay [67]. The numerical analysis of the theoretical results and the processing of the experimental spectra were performed with MATLAB R2016b (The Math Works Inc.) [68].

#### 4. Conclusions

Isotopic substitution leads to much higher variability in NIR spectra as compared with IR spectra, due to significant contribution from the combination bands. The pattern of OH/OD, CH<sub>3</sub>/CD<sub>3</sub>, and CH<sub>2</sub>/CD<sub>2</sub> groups in ethanol often leads to fine spectral changes, which may be monitored and explained in detail by anharmonic quantum mechanical simulations. Our studies were devoted to NIR spectra of eight isotopomers of ethanol (CX<sub>3</sub>CX<sub>2</sub>OX (X = H, D)) by using anharmonic GVPT2 vibrational analysis. The calculations were performed at several levels of electronic theory, including DFT and MP2 to find accurate and efficient theoretical approach for studies of isotopic effect in NIR spectra. Our results indicate that DFT approach using double-hybrid B2PLYP functional, coupled with def2-TZVP basis set, and supported by GD3BJ correction with CPCM solvent model yielded the best results. The theoretical spectra obtained by this approach enabled us to assign most of NIR bands, including two ( $2\nu_x$  and  $\nu_x + \nu_y$ ) and three quanta ( $3\nu_x$ ,  $\nu_x + \nu_y + \nu_z$ , and  $2\nu_x + \nu_y$ ) transitions. Accuracy of these calculations permitted us to analyze theoretical NIR spectra of CH<sub>3</sub>CD<sub>2</sub>OD and CD<sub>3</sub>CH<sub>2</sub>OD for which the experimental spectra are not available. The effect of the isotopic substitution of the OH, CH<sub>3</sub>, and CH<sub>2</sub> groups was satisfactory reproduced and explained. Moreover, the relative contributions of selected groups and kinds of transitions were elucidated and discussed. The contributions from the CH<sub>3</sub> group appear to be more important than those from the CH<sub>2</sub> group. The isotopic substitution in the CH<sub>3</sub> group leads to the most prominent intensity changes in NIR spectra as compared to the changes due to the substitution of the other groups. The bands from the three quanta transitions are more important for isotopomers of ethanol than for derivatives of methanol.

**Supplementary Materials:** The following are available online, Figures S1–S35; Tables S1–S9.

**Author Contributions:** Conceptualization, K.B.B. and M.A.C.; Methodology, K.B.B. and J.G.; Formal analysis, J.G. and K.B.B.; Investigation, all authors; Writing—original draft preparation, K.B.B.; Writing—review and editing, all authors; Supervision, C.W.H. and M.A.C.

**Funding:** This work was supported by the National Science Center Poland, Grant No. 2017/27/B/ST4/00948.

**Acknowledgments:** Calculations have been carried out in Wrocław Centre for Networking and Supercomputing (<http://www.wcss.pl>), under grant no. 163.

**Conflicts of Interest:** The authors declare no conflict of interest. The founders had no role in the design of the study; in the collection, analyses, or interpretation of data; in the writing of the manuscript, or in the decision to publish the results.

#### References

1. Siesler, H.W.; Ozaki, Y.; Kawata, S.; Heise, H.M. (Eds.) *Near-Infrared Spectroscopy*; Wiley-VCH: Weinheim, Germany, 2002.
2. Beć, K.B.; Grabska, J.; Ozaki, Y. Advances in anharmonic methods and their applications to vibrational spectroscopies. In *Frontiers of Quantum Chemistry*; Wójcik, M.J., Nakatsuji, H., Kirtman, B., Ozaki, Y., Eds.; Springer: Singapore, 2017.
3. Beć, K.B.; Grabska, J.; Huck, C.W.; Ozaki, Y. Quantum mechanical simulation of NIR spectra. In *Applications in Physical and Analytical Chemistry*; Ozaki, Y., Wójcik, M.J., Popp, J., Eds.; Wiley: Hoboken, NJ, USA, 2019; in press.
4. Ozaki, Y.; Huck, C.W.; Beć, K.B. Near infrared spectroscopy and its applications. In *Molecular and Laser Spectroscopy*; Gupta, V.P., Ed.; Elsevier: Amsterdam, The Netherlands, 2017.
5. Siesler, H.W. Near-infrared spectra, interpretation. In *Encyclopedia of Spectroscopy and Spectrometry*, 3rd ed.; Lindon, J.C., Tranter, G.E., Koppenaal, D.W., Eds.; Academic Press: Oxford, UK, 2017.
6. Workman, J., Jr.; Weyer, L. *Practical Guide and Spectral Atlas for Interpretive Near-Infrared Spectroscopy*, 2nd ed.; CRC Press: Boca Raton, FL, USA, 2012.
7. Beć, K.B.; Hawranek, J.P. Vibrational analysis of liquid *n*-butylmethylether. *Vib. Spectrosc.* **2013**, *64*, 164–171. [[CrossRef](#)]
8. Beć, K.B.; Kwiatek, A.; Hawranek, J.P. Vibrational analysis of neat liquid *tert*-butylmethylether. *J. Mol. Liq.* **2014**, *196*, 26–31. [[CrossRef](#)]

9. Kirchler, C.G.; Pezzei, C.K.; Beć, K.B.; Henn, R.; Ishigaki, M.; Ozaki, Y.; Huck, C.W. Critical evaluation of NIR and ATR-IR spectroscopic quantifications of rosmarinic acid in rosmarini folium supported by quantum chemical calculations. *Planta Med.* **2017**, *83*, 1076–1084. [[CrossRef](#)] [[PubMed](#)]
10. Beć, K.B.; Huck, C.W. Breakthrough potential in near-infrared spectroscopy: Spectra simulation. A review of recent developments. *Front. Chem.* **2019**, *7*, 1–22. [[CrossRef](#)] [[PubMed](#)]
11. Bozzolo, G.; Plastino, A. Generalized anharmonic oscillator: A simple variational approach. *Phys. Rev. D* **1981**, *24*, 3113–3117.
12. Gribov, L.A.; Prokof'eva, N.I. Variational solution of the problem of anharmonic vibrations of molecules in the central force field. *J. Struct. Chem.* **2015**, *56*, 752–754. [[CrossRef](#)]
13. Bowman, J.M. Self-consistent field energies and wavefunctions for coupled oscillators. *J. Chem. Phys.* **1978**, *68*, 608–610. [[CrossRef](#)]
14. Gerber, R.B.; Chaban, G.M.; Brauer, B.; Miller, Y. *Theory and Applications of Computational Chemistry: The First 40 Years*; Elsevier: Amsterdam, The Netherlands, 2005; pp. 165–193.
15. Jung, J.O.; Gerber, R.B. Vibrational wave functions and spectroscopy of  $(\text{H}_2\text{O})_n$ ,  $n = 2, 3, 4, 5$ : Vibrational self-consistent field with correlation corrections. *J. Chem. Phys.* **1996**, *105*, 10332–10348. [[CrossRef](#)]
16. Norris, L.S.; Ratner, M.A.; Roitberg, A.E.; Gerber, R.B. Møller–Plesset perturbation theory applied to vibrational problems. *J. Chem. Phys.* **1996**, *105*, 11261–11267. [[CrossRef](#)]
17. Monteiro, J.G.S.; Barbosa, A.G.H. VSCF calculations for the intra- and intermolecular vibrational modes of the water dimer and its isotopologs. *Chem. Phys.* **2016**, *479*, 81–90. [[CrossRef](#)]
18. Barone, V.; Biczysko, M.; Bloino, J.; Borkowska-Panek, M.; Carnimeo, I.; Panek, P. Toward Anharmonic Computations of Vibrational Spectra for Large Molecular Systems. *Int. J. Quantum Chem.* **2012**, *112*, 2185–2200. [[CrossRef](#)]
19. Beć, K.B.; Futami, Y.; Wójcik, M.J.; Nakajima, T.; Ozaki, Y. Spectroscopic and computational study of acetic acid and its cyclic dimer in the near-infrared region. *J. Phys. Chem. A* **2016**, *120*, 6170–6183. [[CrossRef](#)]
20. Grabska, J.; Ishigaki, M.; Beć, K.B.; Wójcik, M.J.; Ozaki, Y. Structure and near-infrared spectra of saturated and unsaturated carboxylic acids. An insight from anharmonic DFT calculations. *J. Phys. Chem. A* **2017**, *121*, 3437–3451. [[CrossRef](#)]
21. Grabska, J.; Beć, K.B.; Ishigaki, M.; Wójcik, M.J.; Ozaki, Y. Spectra-structure correlations of saturated and unsaturated medium-chain fatty acids. Near-infrared and anharmonic DFT study of hexanoic acid and sorbic acid. *Spectrochim. Acta A* **2017**, *185*, 35–44. [[CrossRef](#)] [[PubMed](#)]
22. Grabska, J.; Beć, K.B.; Ishigaki, M.; Huck, C.W.; Ozaki, Y. NIR spectra simulations by anharmonic DFT-saturated and unsaturated long-chain fatty acids. *J. Phys. Chem. B* **2018**, *122*, 6931–6944. [[CrossRef](#)] [[PubMed](#)]
23. Biczysko, M.; Bloino, J.; Carnimeo, I.; Panek, P.; Barone, V. Fully ab initio IR spectra for complex molecular systems from perturbative vibrational approaches: Glycine as a test case. *J. Mol. Struct.* **2012**, *1009*, 74–82. [[CrossRef](#)]
24. Biczysko, M.; Bloino, J.; Brancato, G.; Cacelli, I.; Cappelli, C.; Ferretti, A.; Lami, A.; Monti, S.; Pedone, A.; Prampolini, G.; et al. Integrated computational approaches for spectroscopic studies of molecular systems in the gas phase and in solution: Pyrimidine as a test case. *Theor. Chem. Acc.* **2012**, *131*, 1201–1220. [[CrossRef](#)]
25. Beć, K.B.; Karczmit, D.; Kwaśniewicz, M.; Ozaki, Y.; Czarnecki, M.A. Overtones of  $\nu\text{C}\equiv\text{N}$  vibration as a probe of structure of liquid  $\text{CH}_3\text{CN}$ ,  $\text{CD}_3\text{CN}$  and  $\text{CCl}_3\text{CN}$ . Combined IR, NIR, and Raman spectroscopic studies with anharmonic DFT calculations. *J. Phys. Chem. A* **2019**, *123*, 4431–4442. [[CrossRef](#)]
26. Grabska, J.; Beć, K.B.; Kirchler, C.G.; Ozaki, Y.; Huck, C.W. Distinct Difference in Sensitivity of NIR vs. IR Bands of Melamine to Inter-Molecular Interactions with Impact on Analytical Spectroscopy Explained by Anharmonic Quantum Mechanical Study. *Molecules* **2019**, *24*, 1402. [[CrossRef](#)]
27. Beć, K.B.; Grabska, J.; Czarnecki, M.A. Spectra-structure correlations in NIR region: Spectroscopic and anharmonic DFT study of *n*-hexanol, cyclohexanol and phenol. *Spectrochim. Acta A* **2018**, *197*, 176–184. [[CrossRef](#)]
28. Beć, K.B.; Grabska, J.; Kirchler, C.G.; Huck, C.W. NIR spectra simulation of thymol for better understanding of the spectra forming factors, phase and concentration effects and PLS regression features. *J. Mol. Liq.* **2018**, *268*, 895–902. [[CrossRef](#)]
29. Beć, K.B.; Futami, Y.; Wójcik, M.J.; Ozaki, Y. A spectroscopic and theoretical study in the near-infrared region of low concentration aliphatic alcohols. *Phys. Chem. Chem. Phys.* **2016**, *18*, 13666–13682. [[CrossRef](#)]

30. Grabska, J.; Beć, K.B.; Ozaki, Y.; Huck, C.W. Temperature drift of conformational equilibria of butyl alcohols studied by near-infrared spectroscopy and fully anharmonic DFT. *J. Phys. Chem. A* **2017**, *121*, 1950–1961. [[CrossRef](#)]
31. Pele, L.; Gerber, R.B. On the mean accuracy of the separable VSCF approximation for large molecules. *J. Phys. Chem. C* **2010**, *114*, 20603–20608.
32. Otaki, H.; Yagi, K.; Ishiuchi, S.; Fujii, M.; Sugita, Y. Anharmonic Vibrational Analyses of Pentapeptide Conformations Explored with Enhanced Sampling Simulations. *J. Phys. Chem. B* **2016**, *120*, 10199–10213. [[CrossRef](#)]
33. Yagi, K.; Otaki, H.; Li, P.-C.; Thomsen, B.; Sugita, Y. *Weight Averaged Anharmonic Vibrational Calculations: Applications to Polypeptide, Lipid Bilayers, and Polymer Materials*; Ozaki, Y., Wójcik, M.J., Popp, J., Eds.; Wiley: Hoboken, NJ, USA, 2019; in press.
34. Yagi, K.; Yamada, K.; Kobayashi, C.; Sugita, Y. Anharmonic Vibrational Analysis of Biomolecules and Solvated Molecules Using Hybrid QM/MM Computations. *J. Chem. Theory Comput.* **2019**, *15*, 1924–1938. [[CrossRef](#)]
35. Gonjo, T.; Futami, Y.; Morisawa, Y.; Wójcik, M.J.; Ozaki, Y. Hydrogen bonding effects on the wavenumbers and absorption intensities of the OH fundamental and the first, second and third overtones of phenol and 2,6-dihalogenated phenols studied by visible/near-infrared/infrared spectroscopy and density functional theory calculations. *J. Phys. Chem. A* **2011**, *115*, 9845–9853.
36. Futami, Y.; Ozaki, Y.; Hamada, Y.; Wójcik, M.J.; Ozaki, Y. Solvent dependence of absorption intensities and wavenumbers of the fundamental and first overtone of NH stretching vibration of pyrrole studied by near-infrared/infrared spectroscopy and DFT calculations. *J. Phys. Chem. A* **2011**, *115*, 1194–1198. [[CrossRef](#)]
37. Kuenzer, U.; Sorarù, J.-A.; Hofer, T.S. Pushing the limit for the grid-based treatment of Schrödinger's equation: A sparse Numerov approach for one, two and three dimensional quantum problems. *Phys. Chem. Chem. Phys.* **2016**, *18*, 31521–31533. [[CrossRef](#)]
38. Kuenzer, U.; Klotz, M.; Hofer, T.S. Probing vibrational coupling via a grid-based quantum approach—an efficient strategy for accurate calculations of localized normal modes in solid-state systems. *J. Comput. Chem.* **2018**, *39*, 2196–2209. [[CrossRef](#)]
39. Kuenzer, U.; Hofer, T.S. A four-dimensional Numerov approach and its application to the vibrational eigenstates of linear triatomic molecules—The interplay between anharmonicity and inter-mode coupling. *Chem. Phys.* **2019**, *520*, 88–89.
40. Wu, P.; Siesler, H.W. The diffusion of alcohols and water in polyamide 11: A study by FTNIR-spectroscopy. *Macromol. Symp.* **1999**, *143*, 323–336. [[CrossRef](#)]
41. Grabska, J.; Czarnecki, M.A.; Beć, K.B.; Ozaki, Y. Spectroscopic and quantum mechanical calculation study of the effect of isotopic substitution on NIR spectra of methanol. *J. Phys. Chem. A* **2017**, *121*, 7925–7936.
42. Wang, L.; Ishiyama, T.; Morita, A. Theoretical investigation of C–H vibrational spectroscopy. 1. Modeling of methyl and methylene groups of ethanol with different conformers. *J. Phys. Chem. A* **2017**, *121*, 6687–6700. [[CrossRef](#)]
43. Wang, L.; Ishiyama, T.; Morita, A. Theoretical investigation of C–H vibrational spectroscopy. 2. Unified assignment method of IR, Raman, and sum frequency generation spectra of ethanol. *J. Phys. Chem. A* **2017**, *121*, 6701–6712.
44. Bloino, J.; Baiardi, A.; Biczysko, M. Aiming at an accurate prediction of vibrational and electronic spectra for medium-to-large molecules: An overview. *Int. J. Quantum Chem.* **2016**, *116*, 1543–1574.
45. Grimme, S.; Antony, J.; Ehrlich, S.; Krieg, H. A consistent and accurate ab initio parameterization of density functional dispersion correction (DFT-D) for the 94 elements H–Pu. *J. Chem. Phys.* **2010**, *132*, 154104.
46. Fornaro, T.; Biczysko, M.; Monti, S.; Barone, V. Dispersion corrected DFT approaches for anharmonic vibrational frequency calculations: Nucleobases and their dimers. *Phys. Chem. Chem. Phys.* **2014**, *16*, 10112–10128.
47. Matczak, P.; Wojtulewski, S. Performance of Møller-Plesset second-order perturbation theory and density functional theory in predicting the interaction between stannylenes and aromatic molecules. *J. Mol. Model.* **2015**, *21*, 41. [[CrossRef](#)]
48. Kirchler, C.G.; Pezzei, C.K.; Beć, K.B.; Mayr, S.; Ishigaki, M.; Ozaki, Y.; Huck, C.W. Critical evaluation of spectral information of benchtop vs. portable near-infrared spectrometers: Quantum chemistry and two-dimensional correlation spectroscopy for a better understanding of PLS regression models of the rosmarinic acid content in Rosmarini folium. *Analyst* **2017**, *142*, 455–464.

49. Czarnecki, M.A. Effect of temperature and concentration on self-association of octan-1-ol studied by two-dimensional Fourier transform near-infrared correlation spectroscopy. *J. Phys. Chem. A* **2000**, *104*, 6356–6361. [[CrossRef](#)]
50. Czarnecki, M.A. Two-dimensional correlation analysis of the second overtone of the  $\nu(\text{OH})$  mode of octan-1-ol in the pure liquid phase. *Appl. Spectrosc.* **2000**, *54*, 1767–1770. [[CrossRef](#)]
51. Czarnecki, M.A.; Czarnik-Matusewicz, B.; Ozaki, Y.; Iwahashi, M. Resolution enhancement and band assignments for the first overtone of OH(D) stretching modes of butanols by two-dimensional near-infrared correlation spectroscopy. 3. Thermal dynamics of hydrogen bonding in butan-1-(ol-d) and 2-methylpropan-2-(ol-d) in the pure liquid states. *J. Phys. Chem. A* **2000**, *104*, 4906–4911.
52. Czarnecki, M.A.; Maeda, H.; Ozaki, Y.; Suzuki, M.; Iwahashi, M. Resolution enhancement and band assignments for the first overtone of OH stretching mode of butanols by two-dimensional near-infrared correlation spectroscopy. Part I: Sec-butanol. *Appl. Spectrosc.* **1998**, *52*, 994–1000. [[CrossRef](#)]
53. Czarnecki, M.A.; Morisawa, Y.; Futami, Y.; Ozaki, Y. Advances in molecular structure and interaction studies using near-infrared spectroscopy. *Chem. Rev.* **2015**, *115*, 9707–9744. [[CrossRef](#)]
54. Umer, M.; Kopp, W.A.; Leonhard, K. Efficient yet accurate approximations for ab initio calculations of alcohol cluster thermochemistry. *J. Chem. Phys.* **2015**, *143*, 214306. [[CrossRef](#)]
55. Grimme, S. Semiempirical hybrid density functional with perturbative second-order correlation. *J. Chem. Phys.* **2006**, *124*, 034108. [[CrossRef](#)]
56. Weigend, F.; Ahlrichs, R. Balanced basis sets of split valence, triple zeta valence and quadruple zeta valence quality for H to Rn: Design and assessment of accuracy. *Phys. Chem. Chem. Phys.* **2005**, *7*, 3297–3305. [[CrossRef](#)]
57. Grimme, S.; Ehrlich, S.; Goerigk, S.L. Effect of the damping function in dispersion corrected density functional theory. *J. Comput. Chem.* **2011**, *32*, 1456–1465. [[CrossRef](#)]
58. Miertuš, S.; Scrocco, E.; Tomasi, J. Electrostatic interaction of a solute with a continuum. A direct utilization of ab initio molecular potentials for the prevision of solvent effects. *Chem. Phys.* **1981**, *55*, 117–129.
59. Barone, V.; Cossi, M. Quantum calculation of molecular energies and energy gradients in solution by a conductor solvent model. *J. Phys. Chem. A* **1998**, *102*, 1995–2001. [[CrossRef](#)]
60. Barone, V. Anharmonic vibrational properties by a fully automated second-order perturbative approach. *J. Chem. Phys.* **2005**, *122*, 014108. [[CrossRef](#)]
61. Barone, V.; Biczysko, M.; Bloino, J. Fully anharmonic IR and Raman spectra of medium-size molecular systems: Accuracy and interpretation. *Phys. Chem. Chem. Phys.* **2014**, *16*, 1759–1787. [[CrossRef](#)]
62. Frisch, M.J.; Trucks, G.W.; Schlegel, H.B.; Scuseria, G.E.; Robb, M.A.; Cheeseman, J.R.; Scalmani, G.; Barone, V.; Mennucci, B.; Petersson, G.A.; et al. *Gaussian 16, Revision A.03*; Gaussian, Inc.: Wallingford, CT, USA, 2013.
63. Bloino, J.; Biczysko, M. IR and Raman Spectroscopies beyond the Harmonic Approximation: The Second-Order Vibrational Perturbation Theory Formulation. In *Reference Module in Chemistry, Molecular Sciences and Chemical Engineering*; Reedijk, J., Ed.; Elsevier: Waltham, MA, USA, 2015.
64. McQuarrie, D.A. *Statistical Mechanics*; Harper & Row: New York, NY, USA, 1976.
65. Robertson, M.B.; Klein, P.G.; Ward, I.M.; Packer, K.J. NMR study of the energy difference and population of the *gauche* and *trans* conformations in solid polyethylene. *Polymer* **2001**, *42*, 1261–1264. [[CrossRef](#)]
66. Martin, J.M.L.; Van Alsenoy, C. *GAR2PED*; University of Antwerp: Antwerp, Belgium, 1995.
67. Pulay, P.; Fogarasi, G.; Pang, F.; Boggs, J.E. Systematic ab initio gradient calculation of molecular geometries, force constants, and dipole moment derivatives. *J. Am. Chem. Soc.* **1979**, *101*, 2550–2560. [[CrossRef](#)]
68. *MATLAB*; The MathWorks, Inc.: Natick, MA, USA, 2016.

**Sample Availability:** Samples of the compounds ( $\text{CH}_3\text{CH}_2\text{OD}$ ,  $\text{CH}_3\text{CD}_2\text{OH}$ ,  $\text{CD}_3\text{CH}_2\text{OH}$ ,  $\text{CD}_3\text{CD}_2\text{OH}$ ,  $\text{CD}_3\text{CD}_2\text{OD}$ ) are available from the authors.



© 2019 by the authors. Licensee MDPI, Basel, Switzerland. This article is an open access article distributed under the terms and conditions of the Creative Commons Attribution (CC BY) license (<http://creativecommons.org/licenses/by/4.0/>).